Chapter 5
Adaptive BEM-Based Finite Element Method

As long as the solutions of boundary value problems are sufficiently regular, the refinement of the mesh size h and the increase of the approximation order k in the discretization space V_h^k yields an improvement in the accuracy. In particular, this yields optimal convergence rates. But, in most applications the regularity of the solution is restricted due to corners of the domain or jumping physical quantities. Therefore, it is essential to adapt the solution process to the underlying problem in order to retrieve optimal approximation properties. In this chapter, we deal with a posteriori error estimates which can be used to drive an adaptive mesh refinement procedure and we recover optimal rates of convergence for the adaptive methods in the numerical experiments in the presence of singularities. For the error estimation, we cover the classical residual based error estimator as well as goal-oriented techniques on general polytopal meshes. Whereas, we derive reliability and efficiency estimates for the first mentioned estimator, we discuss the benefits and potentials of the second one for general meshes.

5.1 Preliminaries

In the following derivations we restrict ourselves to the model problem and the BEM-based FEM formulation given in Chap. 2. Therefore, let $\Omega \subset \mathbb{R}^d$, $d = 2, 3$ be a polygonal or polyhedral domain. Its boundary $\Gamma = \Gamma_D \cup \Gamma_N$ is split into a Dirichlet and a Neumann part, where we assume $|\Gamma_D| > 0$. Given a source term $f \in L_2(\Omega)$, a Dirichlet datum $g_D \in H^{1/2}(\Gamma_D)$ as well as a Neumann datum $g_N \in L_2(\Gamma_N)$, the

© Springer Nature Switzerland AG 2019

S. Weißer, *BEM-based Finite Element Approaches on Polytopal Meshes*,
Lecture Notes in Computational Science and Engineering 130,
https://doi.org/10.1007/978-3-030-20961-2_5

problem reads

$$\begin{aligned} -\operatorname{div}(a\nabla u) &= f \quad \text{in } \Omega \ , \\ u &= g_D \quad \text{on } \Gamma_D \ , \\ a\nabla u \cdot \mathbf{n} &= g_N \quad \text{on } \Gamma_N \ . \end{aligned}$$

Furthermore, we restrict ourselves for the presentation in this chapter to piecewise constant diffusion coefficients which are aligned with the mesh, i.e.

$$a(\mathbf{x}) = a_K \quad \text{for } \mathbf{x} \in K \text{ and } K \in \mathscr{K}_h$$

for the initial mesh and consequently for all meshes in the refinement process. The Galerkin as well as the corresponding discrete Galerkin formulation are given in Sect. 2.5. We assume for simplicity, that the extension of the Dirichlet data g_D can be chosen in V_h^k. The Galerkin formulations thus read

$$\begin{aligned} &\text{Find } u \in g_D + H_D^1(\Omega) : \\ &b(u,v) = (f,v)_{L_2(\Omega)} + (g_N,v)_{L_2(\Gamma_N)} \quad \forall v \in H_D^1(\Omega) \ , \end{aligned} \tag{5.1}$$

and

$$\begin{aligned} &\text{Find } u_h \in g_D + V_{h,D}^k : \\ &b(u_h,v_h) = (f,v_h)_{L_2(\Omega)} + (g_N,v_h)_{L_2(\Gamma_N)} \quad \forall v_h \in V_{h,D}^k \ . \end{aligned} \tag{5.2}$$

In Chap. 2, the approximation spaces are defined and we have derived a priori error estimates for the Galerkin approximation $u_h \in V_h^k$ of the form

$$\|u - u_h\|_{H^1(\Omega)} \le c\, h^k\, |u|_{H^{k+1}(\Omega)} \quad \text{for } u \in H^{k+1}(\Omega) \ . \tag{5.3}$$

As already mentioned, the convergence rate k in these estimates is linked to, and restricted by the regularity of the solution $u \in H^{k+1}(\Omega)$. Furthermore, the estimate cannot be evaluated for computational purposes since it contains the unknown solution u in the right hand side. The aim of an adaptive FEM is to retrieve the convergence $\mathscr{O}(h^k)$, $k \in \mathbb{N}$ of the error although the exact solution is not regular at all, i.e. $u \notin H^2(\Omega)$. In order to achieve this, we need an error estimator that is computable and can serve as an indicator for local refinement. We consider estimates of the form

$$\|u - u_h\| \le c\, \eta \quad \text{for} \quad \eta^2 = \sum_{K \in \mathscr{K}_h} \eta_K^2 \ ,$$

where $\eta = \eta(u_h)$ is desirable for practical considerations. Here, $\|\cdot\|$ denotes some norm and η is a computable error estimator, which depends on the current approximation u_h but not on the unknown solution u explicitly. Therefore, the inequality is called a posteriori error estimate. The values η_K, which are assigned to the elements $K \in \mathscr{K}_h$, serve as error indicator over the corresponding elements. With their help, we can monitor the approximation quality over the single elements and we can use this information for local mesh refinement.

The preceding considerations lead to an adaptive finite element strategy, which is often abbreviated to AFEM in the literature. This scheme can be sketched as

$$\textbf{SOLVE} \rightarrow \textbf{ESTIMATE} \rightarrow \textbf{MARK} \rightarrow \textbf{REFINE} \rightarrow \textbf{SOLVE} \rightarrow \cdots .$$

First, the discrete boundary value problem is solved on a given mesh and the error estimator η and the error indicators η_K are computed for all elements. If the desired accuracy is reached according to η, we are done. If not, some elements are marked for refinement. These elements are chosen on the basis of the error indicators η_K. Next, the marked elements are refined, and thus we obtain a new mesh which is adapted to the problem. Afterwards, we can solve the boundary value problem on the refined mesh and continue this procedure until the desired accuracy is reached.

For triangular meshes and piecewise linear trial functions, the first convergence proof for the adaptive finite element method applied to the Poisson problem can be found in [67]. Here, the mesh has to satisfy some fineness assumption. In [129], this condition is removed and the notion of data oscillation is introduced. A general convergence result for conforming adaptive finite elements, which is valid for several error estimates and for a class of problems, has been published 7 years later in [130]. The first convergence rates are proven in [36], where an additional coarsening step is introduced and the refinement is done in such a way that a new node lies inside each marked element of the previous mesh. In [55], the authors show a decay rate of the energy error plus data oscillation in terms of the number of degrees of freedom without the additional assumptions on coarsening and refining. A state of the art discussion and an axiomatic presentation of the proof of optimal convergence rates of adaptive finite element methods can be found in [53].

Whereas the cited theory is done for triangular meshes, we state an adaptive finite element method on regular and stable polygonal meshes. In the **SOLVE** step, we approximate the solution of the boundary value problem on the current mesh $\mathscr{K}_h$. This is done as described in Chap. 2. Solving the discrete problem, we obtain an approximation $u_h \in V_h^k$ on the current mesh for a fixed order k.

The **ESTIMATE** part serves for the computation of the a posteriori error estimator η and local error indicators η_K. There is a great variety of estimators in the literature. The most classical one is the residual error estimate which goes back to [15]. This estimator measures the jumps of the conormal derivative of the approximation u_h over the element boundaries. Other estimators are obtained by solving local Dirichlet [16] or Neumann [19] problems on element patches. The engineering community came up with an error indicator that uses the difference between ∇u_h and its continuous approximation, see [183]. The equilibrated residual error estimator [39] is obtained by post-processing of the approximation and belongs

to the more general class of functional analytic error estimates [142]. Finally, we mention the hierarchical [64] and the goal oriented [18] error estimates. For a comparison of all these strategies see for instance [54].

After the computation of the estimator and the local error indicators, we have to **MARK** several elements for refinement. There are different strategies in the literature for this task. The most classical one is the *maximum strategy* which has been proposed already in [16]. Here, all elements $K \in \mathscr{K}_h$ are marked which satisfy

$$\eta_K \geq \theta \ \eta_{\max}$$

for a given parameter $0 \leq \theta \leq 1$ and $\eta_{\max} = \max\{\eta_K : K \in \mathscr{K}_h\}$. So, the elements with the largest error indicators are chosen for refinement. For large values of θ, the strategy becomes more selective, whereas for small θ, we obtain almost a uniform refinement. A similar idea is used by the modified *equidistribution strategy*. For a given parameter $0 \leq \theta \leq 1$ and the global error estimator η, all elements $K \in \mathscr{K}_h$ are marked which satisfy

$$\eta_K \geq \theta \ \frac{\eta}{\sqrt{|\mathscr{K}_h|}} \ .$$

In this strategy one tries to reach a state where the error is distributed equally over all elements. The parameter θ controls again the selectivity. This kind of strategy has been used in Sect. 3.4.6 for the generation of anisotropically adapted meshes. Finally, we mention *Dörfler's strategy*, see [67]. Here, a set of elements $\mathscr{K}_M \subset \mathscr{K}_h$ is marked such that

$$\Big(\sum_{K \in \mathscr{K}_M} \eta_K^2 \Big)^{1/2} \geq (1-\theta) \ \eta \ ,$$

where $0 \leq \theta < 1$ is again a given parameter and η the global estimator. It is advantageous to choose the set $\mathscr{K}_M$ as small as possible. This can be achieved by sorting the elements $K \in \mathscr{K}_h$ according to the value of their error indicators η_K. Since every sorting algorithm is computationally expensive, Dörfler proposed in [67] the following procedure with given parameter $0 < \nu < 1$, which is chosen to be small.

```
sum = 0.0
μ = 1.0
while (sum < (1-θ)² η²)
do
  μ = μ - ν
  for all K ∈ 𝒦_h
    if (K is not marked)
      if (η_K > μ η_max)
        mark K
        sum = sum + η_K²
```

Dörfler's marking strategy was one of the key points in the proofs of convergence and convergence rates of AFEM in the literature mentioned above.

As the name of the last step **REFINE** already indicates, this is the time where the marked elements are refined. Usually, this step is more complicated for standard methods working on triangular or quadrangular meshes because of the strict admissibility conditions on the mesh. In such cases, it has to be guaranteed that no hanging nodes appear. Therefore, the mesh has to be completed in the sense that neighbouring elements are refined until all hanging nodes disappear. In the literature, one can find several strategies like red-green refinement or newest vertex bisection with completion algorithms, see [36, 170]. Another possibility to handle hanging nodes is to treat them as conditional degrees of freedom, i.e., to fix the value of the finite element functions in these points to be a suitable interpolation of their neighbouring regular nodes. Nevertheless, the first idea with completion spreads the local refinement into a neighbourhood and the second one produces artificial nodes. Both scenarios are somehow unpleasant for the numerical realization. Due to the use of the BEM-based FEM, we are in the fortune situation to cope with arbitrary polytopal meshes. Therefore, we do not have to worry about hanging nodes because they are incorporated as ordinary nodes in the strategy and thus contribute to the approximation accuracy. This behaviour is discussed more precisely in Sect. 5.2.3. The refinement only affects the marked elements and is done as described in Sect. 2.2.3. During this refinement process with the discussed bisection algorithm, the stability of the sequence of meshes is not preserved automatically. Thus, we might want to enforce this property explicitly in the mesh refinement.

In certain algorithms and applications an additional **COARSEN** step is necessary which reverses the local mesh refinement in some areas of the domain. This has been introduced in [36] for theoretical reasons in order to prove convergence rates for the adaptive algorithm. But also in time-dependent problems, this additional step is meaningful if, for instance, the singularity of the solution travels through the spacial domain. The coarsening often relies on the hierarchy of adaptive meshes obtained during the refinement. For polytopal meshes, however, one might agglomerate almost arbitrary elements in this step since the union of polytopes is a polytope. This demonstrates once more the flexibility of these general meshes.

5.2 Residual Based Error Estimator

In this section, we consider one of the most classical a posteriori error estimators, namely the residual based error estimator, and formulate it on polytopal meshes. For the classical results on simplicial meshes see, e.g., [4, 170]. This a posteriori error estimate bounds the difference of the exact solution and the Galerkin approximation in the energy norm $\|\cdot\|_b$ associated to the symmetric and positive definite bilinear form, i.e. $\|\cdot\|_b^2 = b(\cdot,\cdot)$. Among others, the estimate contains the jumps of the conormal derivatives over the element interfaces. Since we are dealing with the three- and two-dimensional case simultaneously, $F \in \mathscr{F}_h$ denotes a face ($d = 3$) or

edge ($d = 2$), respectively. Such a jump over an internal face $F \in \mathscr{F}_{h,\Omega}$ is defined by

$$[\![u_h]\!]_F = \left(a_K \gamma_1^K u_h + a_{K'} \gamma_1^{K'} u_h \right) \Big|_F ,$$

where $K, K' \in \mathscr{K}_h$ are the neighbouring elements of F with $F \in \mathscr{F}(K) \cap \mathscr{F}(K')$. The element residual is given by

$$R_K = f + a_K \Delta u_h \quad \text{for } K \in \mathscr{K}_h ,$$

and the face/edge residual by

$$R_F = \begin{cases} 0 & \text{for } F \in \mathscr{F}_{h,D} , \\ g_N - a_K \gamma_1^K u_h & \text{for } F \in \mathscr{F}_{h,N} \text{ with } F \in \mathscr{F}(K) , \\ -\frac{1}{2} [\![u_h]\!]_F & \text{for } F \in \mathscr{F}_{h,\Omega} . \end{cases}$$

We can proceed as for the two-dimensional case in [174, 180] in order to formulate the residual based error estimator and to prove its reliability and efficiency on polytopal meshes. This estimator involves the previously defined element and face residuals and gives an upper bound for the Galerkin error in the energy norm which does not contain any unknown quantity.

Theorem 5.1 (Reliability) *Let $\mathscr{K}_h$ be a regular and stable mesh. Furthermore, let $u \in g_D + H_D^1(\Omega)$ and $u_h \in g_D + V_{h,D}^k$ be the solutions of (5.1) and (5.2), respectively. The residual based error estimate is reliable, i.e.*

$$\|u - u_h\|_b \leq c \, \eta_R \quad \textit{with} \quad \eta_R^2 = \sum_{K \in \mathscr{K}_h} \eta_K^2 ,$$

where the error indicator is defined by

$$\eta_K^2 = h_K^2 \|R_K\|_{L_2(K)}^2 + \sum_{F \in \mathscr{F}(K)} h_F \|R_F\|_{L_2(F)}^2 .$$

The constant $c > 0$ only depends on the regularity and stability parameters of the mesh, see Sect. 2.2, the approximation order k, the space dimension d and on the diffusion coefficient a.

In this presentation it is assumed that we can compute $\gamma_1^K u_h$ analytically. However, in the realization these terms are treated by means of boundary element methods as discussed in Chap. 4. This approximation of the Neumann traces has been incorporated in [180] and yields an additional term in the estimate.

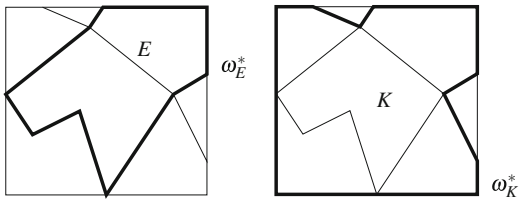

Fig. 5.1 Example of modified neighbourhoods of edges and elements in two space dimensions, cf. Fig. 3.1

Whereas the reliability gives an upper bound for the error, the efficiency states a local upper bound for the error indicator in terms of the approximation error and the problem data. Beside of the neighbourhoods (3.2) of nodes, edges, faces and elements defined in Sect. 3.1, we additionally need the following modified versions

$$\overline{\omega}_E^* = \bigcup_{K' \in \mathscr{K}_h : E \in \mathscr{E}(K')} \overline{K'}\,, \qquad \overline{\omega}_F^* = \bigcup_{K' \in \mathscr{K}_h : F \in \mathscr{F}(K')} \overline{K'}\,, \qquad \overline{\omega}_K^* = \bigcup_{F \in \mathscr{F}(K)} \overline{\omega}_F^*\,, \tag{5.4}$$

cf. Fig. 5.1. Furthermore, we introduce the notation $\|\cdot\|_{b,\omega}$ for $\omega \subset \Omega$, which means that the energy norm is only computed over the subset ω. More precisely, it is $\|v\|_{b,\omega}^2 = (a\nabla v, \nabla v)_{L_2(\omega)}$ for our model problem.

Theorem 5.2 (Efficiency) *Under the assumptions of Theorem 5.1, the residual based error indicator is efficient, i.e.*

$$\eta_K \le c \left(\|u - u_h\|_{b,\omega_K^*}^2 + h_K^2 \|f - \widetilde{f}\|_{L_2(\omega_K^*)}^2 + \sum_{F \in \mathscr{F}(K) \cap \mathscr{F}_{h,N}} h_F \|g_N - \widetilde{g}_N\|_{L_2(F)}^2 + h_K \sum_{K' \subset \omega_K^*} \|\gamma_1^{K'} u_h - \widetilde{\gamma_1^{K'} u_h}\|_{L_2(\partial K')}^2 \right)^{1/2},$$

where $\widetilde{f}$, $\widetilde{g}_N$ and $\widetilde{\gamma_1^{K'} u_h}$ are piecewise polynomial approximations of f, g_N and $\gamma_1^{K'} u_h$, respectively. The constant $c > 0$ only depends on the regularity and stability parameters of the mesh, see Sect. 2.2, the approximation order k, the space dimension d and on the diffusion coefficient a.

The terms involving the data approximation $\|f - \widetilde{f}\|_{L_2(\omega_K^*)}$ and $\|g_N - \widetilde{g}_N\|_{L_2(F)}$ are often called data oscillations. They are usually of higher order. Additionally, we have the term $\|\gamma_1^{K'} u_h - \widetilde{\gamma_1^{K'} u_h}\|_{L_2(\partial K')}$ measuring oscillations in the Neumann trace of the approximation u_h on the boundaries of the elements. The piecewise polynomial function $\widetilde{\gamma_1^{K'} u_h}$ might be chosen as the approximation of the Neumann trace obtained as solution of the derived boundary integral equation from Chap. 4. Thus, known error estimates from the boundary element method can be applied in order to bound this term further if needed.

Remark 5.3 Under certain conditions on the diffusion coefficient it is possible to get the estimates in Theorems 5.1 and 5.2 robust with respect to a, see, e.g., [139].

5.2.1 Reliability

We follow the classical lines in the proof of the reliability, see, e.g., [170]. However, we have to take care on the polytopal elements and the quasi-interpolation operators.

Proof (Theorem 5.1) The bilinear form $b(\cdot,\cdot)$ is a inner product on $V = H^1_D(\Omega)$ due to its boundedness and ellipticity, and thus, V is a Hilbert space together with $b(\cdot,\cdot)$ and $\|\cdot\|_b$. The Riesz representation theorem yields

$$\|u - u_h\|_b = \sup_{v\in V\setminus\{0\}} \frac{|\mathfrak{R}(v)|}{\|v\|_b} \quad \text{with} \quad \mathfrak{R}(v) = b(u-u_h, v)\ . \tag{5.5}$$

Thus, in order to prove the theorem, we reformulate and estimate the term $|\mathfrak{R}(v)|$ in the following. Let $v_h \in V^1_{h,D}$, the Galerkin orthogonality $b(u-u_h, v_h) = 0$ and integration by parts over each element lead to

$$\mathfrak{R}(v) = \sum_{K\in\mathscr{K}_h} \Big((R_K, v - v_h)_{L_2(K)} + \sum_{F\in\mathscr{F}(K)} (R_F, v - v_h)_{L_2(F)} \Big)\ . \tag{5.6}$$

The Cauchy–Schwarz inequality yields

$$|\mathfrak{R}(v)| \le \sum_{K\in\mathscr{K}_h} \Big(\|R_K\|_{L_2(K)} \|v - v_h\|_{L_2(K)} + \sum_{F\in\mathscr{F}(K)} \|R_F\|_{L_2(F)} \|v - v_h\|_{L_2(F)} \Big)\ .$$

We choose $v_h = \mathfrak{I}_C v$, where $\mathfrak{I}_C$ is the Clément interpolation operator from Sect. 3.3, which preserves the homogeneous boundary data on Γ_D. Estimating the L_2-norms of $v - \mathfrak{I}_C v$ over the elements and faces with the help of Theorem 3.7, we find

$$\begin{aligned} |\mathfrak{R}(v)| &\le c \sum_{K\in\mathscr{K}_h} \Big(h_K \|R_K\|_{L_2(K)} |v|_{H^1(\omega_K)} + \sum_{F\in\mathscr{F}(K)} h_F^{1/2} \|R_F\|_{L_2(F)} |v|_{H^1(\omega_F)} \Big) \\ &\le c \Big(\sum_{K\in\mathscr{K}_h} \eta_K^2 \Big)^{1/2} \Big(\sum_{K\in\mathscr{K}_h} |v|^2_{H^1(\omega_K)} \Big)^{1/2} \le c\ \eta_R\ |v|_{H^1(\Omega)}\ , \end{aligned}$$

where in the last two estimates we utilized several times Cauchy–Schwarz inequality and the facts, that each element has a bounded number of faces, see Lemmata 2.7 and 2.16, and that it is covered by a uniformly bounded number of patches only, see Lemma 3.1. Because of $\sqrt{a/a_{\min}} > 1$, it is $|v|_{H^1(\Omega)} \le \|v\|_b / \sqrt{a_{\min}}$ and thus (5.5) together with the previous inequality completes the proof. □

5.2.2 *Efficiency*

The classical proof of efficiency for the residual based error estimator makes use of special bubble functions over the simplicial meshes. These functions have support over single elements and are used to localize the residuals. We adapt the bubble function technique to polytopal meshes. Therefore, let ϕ_T and ϕ_F be the usual polynomial bubble functions over the auxiliary discretization $\mathscr{T}_h(\mathscr{K}_h)$ consisting of triangles ($d = 2$) or tetrahedra ($d = 3$), see [4, 170]. Here, ϕ_T is a cubic ($d = 2$) or quartic ($d = 3$) polynomial over the triangle/tetrahedron $T \in \mathscr{T}_h(\mathscr{K}_h)$, which vanishes on $\Omega \setminus T$ and in particular on ∂T. It is usually defined as the product of the barycentric coordinates of the triangle and tetrahedron, respectively, and scaled such that its maximum is one. The edge bubble ϕ_F is a piecewise quadratic ($d = 2$) or cubic ($d = 3$) polynomial over the adjacent triangles/tetrahedra in $\mathscr{T}_h(\mathscr{K}_h)$, sharing the common edge/face F, and it vanishes elsewhere. This bubble function can also be defined as scaled product of barycentric coordinates.

At first glance, we might define the bubble functions over polytopes as product of the first order basis functions defined in Sect. 2.3.1 or one might use the element bubble functions defined in Sect. 2.3.2. However, in these cases the functions are no polynomials that complicates their treatment in the analysis. In contrast, we define the new bubble functions over the polytopal mesh with the help of the bubble functions over the auxiliary discretization, namely

$$\varphi_K = \sum_{T \in \mathscr{T}_h(K)} \phi_T \qquad \text{and} \qquad \varphi_F = \phi_F$$

for $K \in \mathscr{K}_h$ and $F \in \mathscr{F}_h$.

Lemma 5.4 *Let $K \in \mathscr{K}_h$ and $F \in \mathscr{F}(K)$ of a regular and stable mesh $\mathscr{K}_h$. The bubble functions satisfy*

$$\begin{aligned} \operatorname{supp} \varphi_K &= K\,, \quad 0 \le \varphi_K \le 1\,, \\ \operatorname{supp} \varphi_F &\subset \omega_F^*\,, \quad 0 \le \varphi_F \le 1\,, \end{aligned}$$

and fulfil for $p \in \mathscr{P}^k(K)$ the estimates

$$\begin{aligned} \|p\|^2_{L_2(K)} &\le c\,(\varphi_K p, p)_{L_2(K)}\,, & |\varphi_K p|_{H^1(K)} &\le c h_K^{-1}\,\|p\|_{L_2(K)}\,, \\ \|p\|^2_{L_2(F)} &\le c\,(\varphi_F p, p)_{L_2(F)}\,, & |\varphi_F p|_{H^1(K)} &\le c h_F^{-1/2}\,\|p\|_{L_2(F)}\,, \\ & & \|\varphi_F p\|_{L_2(K)} &\le c h_F^{1/2}\,\|p\|_{L_2(F)}\,. \end{aligned}$$

The constants $c > 0$ only depend on the regularity and stability parameters of the mesh, see Sect. 2.2, the approximation order k and the space dimension d.

Proof Similar estimates are valid for ϕ_T and ϕ_F on triangular and tetrahedral meshes, see [4, 170]. By the use of Cauchy–Schwarz inequality and the properties of the auxiliary discretization $\mathscr{T}_h(\mathscr{K}_h)$ the estimates translate to the new bubble functions. The details of the proof are omitted. □

With these ingredients the proof of Theorem 5.2 can be addressed. The arguments follow the line of [4].

Proof (Theorem 5.2) Let $\widetilde{R}_K \in \mathscr{P}^k(K)$ be a polynomial approximation of the element residual R_K for $K \in \mathscr{K}_h$. For $v = \varphi_K \widetilde{R}_K \in H_0^1(K)$ and $v_h = 0$ Eq. (5.6) yields

$$b(u - u_h, \varphi_K \widetilde{R}_K) = \Re(\varphi_K \widetilde{R}_K) = (R_K, \varphi_K \widetilde{R}_K)_{L_2(K)} .$$

Lemma 5.4 gives

$$\begin{aligned} \|\widetilde{R}_K\|^2_{L_2(K)} &\le c\,(\varphi_K \widetilde{R}_K, \widetilde{R}_K)_{L_2(K)} \\ &= c\left((\varphi_K \widetilde{R}_K, \widetilde{R}_K - R_K)_{L_2(K)} + (\varphi_K \widetilde{R}_K, R_K)_{L_2(K)}\right) \\ &\le c\left(\|\widetilde{R}_K\|_{L_2(K)} \|\widetilde{R}_K - R_K\|_{L_2(K)} + b(u - u_h, \varphi_K \widetilde{R}_K)\right) , \end{aligned}$$

and furthermore,

$$b(u-u_h, \varphi_K \widetilde{R}_K) \le c\,|u-u_h|_{H^1(K)} |\varphi_K \widetilde{R}_K|_{H^1(K)} \le c h_K^{-1}\, \|u-u_h\|_{b,K} \|\widetilde{R}_K\|_{L_2(K)} .$$

We thus get

$$\|\widetilde{R}_K\|_{L_2(K)} \le c\left(h_K^{-1} \|u - u_h\|_{b,K} + \|\widetilde{R}_K - R_K\|_{L_2(K)}\right) ,$$

and by the reverse triangle inequality

$$\|R_K\|_{L_2(K)} \le c\left(h_K^{-1} \|u - u_h\|_{b,K} + \|\widetilde{R}_K - R_K\|_{L_2(K)}\right) .$$

Next, we consider the face residual. Let $\widetilde{R}_F \in \mathscr{P}^k(F)$ be an approximation of R_F, with $F \in \mathscr{F}_{h,\Omega}$. The case $F \in \mathscr{F}_{h,N}$ is treated analogously. For $v = \varphi_F \widetilde{R}_F \in H_0^1(\omega_F^*)$ and $v_h = 0$ Eq. (5.6) yields in this case

$$b(u-u_h, \varphi_F \widetilde{R}_F) = \Re(\varphi_F \widetilde{R}_F) = \sum_{K \subset \omega_F^*} \left((R_K, \varphi_F \widetilde{R}_F)_{L_2(K)} + (R_F, \varphi_F \widetilde{R}_F)_{L_2(F)}\right) .$$

Applying Lemma 5.4 and the previous formula leads to

$$\begin{aligned}\|\widetilde{R}_F\|^2_{L_2(F)} &\le c\,(\varphi_F\widetilde{R}_F,\widetilde{R}_F)_{L_2(F)}\\ &= c\left((\varphi_F\widetilde{R}_F,\widetilde{R}_F-R_F)_{L_2(F)}+(\varphi_F\widetilde{R}_F,R_F)_{L_2(F)}\right)\\ &\le c\left(\|\widetilde{R}_F\|_{L_2(F)}\|\widetilde{R}_F-R_F\|_{L_2(F)}+(\varphi_F\widetilde{R}_F,R_F)_{L_2(F)}\right)\,,\end{aligned}$$

and

$$\begin{aligned}|(\varphi_F\widetilde{R}_F,R_F)_{L_2(F)}| &= \tfrac{1}{2}\left|b(u-u_h,\varphi_F\widetilde{R}_F)-\sum_{K\subset\omega_F^*}(R_K,\varphi_F\widetilde{R}_F)_{L_2(K)}\right|\\ &\le c\left(|u-u_h|_{H^1(\omega_F^*)}|\varphi_F\widetilde{R}_F|_{H^1(\omega_F^*)}+\sum_{K\subset\omega_F^*}\|R_K\|_{L_2(K)}\|\varphi_F\widetilde{R}_F\|_{L_2(K)}\right)\\ &\le c\left(h_F^{-1/2}\|u-u_h\|_{b,\omega_F^*}+\sum_{K\subset\omega_F^*}h_F^{1/2}\|R_K\|_{L_2(K)}\right)\|\widetilde{R}_F\|_{L_2(F)}\,.\end{aligned}$$

Therefore, it is

$$\|\widetilde{R}_F\|_{L_2(F)} \le c\left(h_F^{-1/2}\|u-u_h\|_{b,\omega_F^*}+\sum_{K\subset\omega_F^*}h_F^{1/2}\|R_K\|_{L_2(K)}+\|\widetilde{R}_F-R_F\|_{L_2(F)}\right).$$

By the reverse triangle inequality, $h_K^{-1} \le h_F^{-1}$ and the previous estimate for $\|R_K\|_{L_2(K)}$, we obtain

$$\|R_F\|_{L_2(F)} \le c\left(h_F^{-1/2}\|u-u_h\|_{b,\omega_F^*}+\sum_{K\subset\omega_F^*}h_F^{1/2}\|\widetilde{R}_K-R_K\|_{L_2(K)}+\|\widetilde{R}_F-R_F\|_{L_2(F)}\right).$$

Let $\widetilde{f}$, $\widetilde{g}_N$ and $\widetilde{\gamma_1^K u_h}$ be piecewise polynomial approximations of f, g_N and $\gamma_1^K u_h$, respectively. We choose $\widetilde{R}_K = \widetilde{f} + a_K\Delta u_h$ for $K \in \mathscr{K}_h$ and

$$\widetilde{R}_F = \begin{cases} 0 & \text{for } F \in \mathscr{F}_{h,D}\,,\\ \widetilde{g}_N - a_K\widetilde{\gamma_1^K u_h} & \text{for } F \in \mathscr{F}_{h,N} \text{ with } F \in \mathscr{F}(K)\,,\\ -\frac{1}{2}\left(a_K\widetilde{\gamma_1^K u_h}+a_{K'}\widetilde{\gamma_1^{K'} u_h}\right) & \text{for } F \in \mathscr{F}_{h,\Omega} \text{ with } F \subset \mathscr{F}(K)\cap\mathscr{F}(K')\,.\end{cases}$$

Consequently, we have $\widetilde{R}_K \in \mathscr{P}^k(K)$ and $\widetilde{R}_F \in \mathscr{P}^k(F)$. Finally, the estimates for $\|R_K\|_{L_2(K)}$ and $\|R_F\|_{L_2(F)}$ yield after some applications of the Cauchy–Schwarz

inequality and due to $h_F \leq h_K$ and $|\mathscr{F}(K)| \leq c$, see Lemmata 2.7 and 2.16,

$$\begin{aligned}\eta_K^2 &\leq c\left(\|u-u_h\|_{b,\omega_K^*}^2 + h_K^2 \sum_{K'\subset\omega_K^*} \|\widetilde{R}_{K'} - R_{K'}\|_{L_2(K')}^2 + \sum_{F\in\mathscr{F}(K)} h_F \|\widetilde{R}_F - R_F\|_{L_2(F)}^2\right)\\ &\leq c\left(\|u-u_h\|_{b,\omega_K^*}^2 + h_K^2 \|f-\widetilde{f}\|_{L_2(\omega_K^*)}^2\right.\\ &\qquad \left. + \sum_{F\in\mathscr{F}(K)\cap\mathscr{F}_{h,N}} h_F \|g_N - \widetilde{g}_N\|_{L_2(F)}^2 + h_K \sum_{K'\subset\omega_K^*} \|\gamma_1^{K'} u_h - \widetilde{\gamma_1^{K'} u_h}\|_{L_2(\partial K')}^2\right).\end{aligned}$$

□

5.2.3 Numerical Experiments

The residual based error estimate can be used as stopping criteria to check if the desired accuracy is reached in a simulation on a sequence of meshes. However, it is well known that residual based estimators overestimate the true error a lot. But, because of the equivalence of the norms $\|\cdot\|_{1,\Omega}$ and $\|\cdot\|_b$ on $H_D^1(\Omega)$, we can still use η_R to verify numerically the convergence rates for uniform mesh refinement when $h \to 0$. On the other hand, we can utilize the error indicators in order to gauge the approximation quality over the single elements and drive an adaptive mesh refinement strategy with this information. The adaptive algorithm discussed in Sect. 5.1, has been implemented with Dörfler's marking strategy. During the refinement of the mesh we enforce the stability condition. This is done by refining elements that do not satisfy $h_K < c_T h_E$ for a threshold parameter c_T.

In the following we present numerical examples in 2-dimensions on uniformly and adaptively refined meshes. For the convergence analysis, we consider the error with respect to the mesh size $h = \max\{h_K : K \in \mathscr{K}_h\}$ for uniform refinement. For the adaptive BEM-based FEM, the convergence is studied with respect to the number of degrees of freedom (DoF). On uniform meshes the relation $\text{DoF} = \mathscr{O}(h^{-2})$ holds, whereas on adaptive meshes the mesh size does not decrease uniformly.

Experiment 1: Uniform Refinement Strategy
Consider the Dirichlet boundary value problem

$$-\Delta u = f \quad \text{in } \Omega = (0,1)^2\,, \qquad u = 0 \quad \text{on } \Gamma\,,$$

where $f \in L_2(\Omega)$ is chosen in such a way that $u(\mathbf{x}) = \sin(\pi x_1)\sin(\pi x_2)$ for $\mathbf{x} \in \Omega$ is the exact solution. The solution is smooth, and thus, we expect optimal rates of convergence for uniform mesh refinement. The problem is treated with the BEM-based FEM for different approximation orders $k = 1, 2, 3$ on a sequence of meshes with L-shaped elements of decreasing diameter, see Fig. 5.2 left. In Fig. 5.3, we

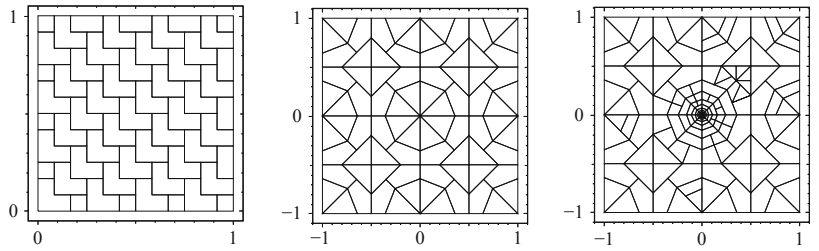

Fig. 5.2 Mesh with L-shaped elements for uniform refinement (left), initial mesh for adaptive refinement (middle), adaptive refined mesh after 30 steps for $k = 2$ with solution having a singularity in the origin of the coordinate system (right)

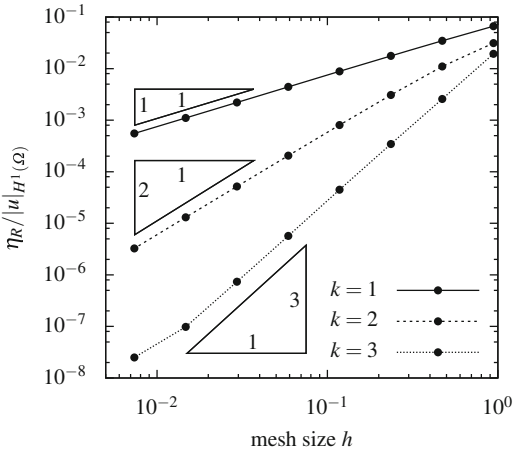

Fig. 5.3 Convergence graph for sequence of uniform meshes with L-shaped elements and V_h^k, $k = 1, 2, 3$, where $\eta_R/|u|_{H^1(\Omega)}$ is given with respect to h in logarithmic scale

give the convergence graphs in logarithmic scale for the value $\eta_R/|u|_{H^1(\Omega)}$, which behaves like the relative H^1-error, with respect to the mesh size h. The example confirms the theoretical rates of convergence stated in Sect. 2.5 on a sequence of meshes with non-convex elements. The highly accurate computations for V_h^3 involve approximately 690,000 degrees of freedom. Due to the decoupling of the variational formulation discussed in Sect. 2.5 into (2.31) and (2.32) the global system of linear equations has about 540,000 unknowns and the remaining degrees of freedom are determined by local projections.

Experiment 2: Adaptive Refinement for Solution with Singularity
Let $\Omega = (-1, 1)^2 \subset \mathbb{R}^2$ be split into two domains, $\Omega_1 = \Omega \setminus \overline{\Omega}_2$ and $\Omega_2 = (0, 1)^2$. Consider the boundary value problem

$$-\operatorname{div}(a\nabla u) = 0 \quad \text{in } \Omega\,, \qquad u = g_D \quad \text{on } \Gamma\,,$$

where the coefficient a is given by

$$a = \begin{cases} 1 \text{ in } \Omega_1\,, \\ 100 \text{ in } \Omega_2\,. \end{cases}$$

Using polar coordinates (r, ϕ) such that $\mathbf{x} = (r\cos\phi, r\sin\phi)^\top$, we choose the boundary data as restriction of the global function

$$g_D(\mathbf{x}) = r^\lambda \begin{cases} \cos(\lambda(\phi - \pi/4)) \text{ for } \mathbf{x} \in \mathbb{R}^2_+, \\ \beta\cos(\lambda(\pi - |\phi - \pi/4|)) \text{ else,} \end{cases}$$

with

$$\lambda = \frac{4}{\pi}\arctan\left(\sqrt{\frac{103}{301}}\right) \quad \text{and} \quad \beta = -100\frac{\sin\left(\lambda\frac{\pi}{4}\right)}{\sin\left(\lambda\frac{3\pi}{4}\right)}\,.$$

This problem is constructed in such a way that $u = g_D$ is the exact solution in Ω. Due to the ratio of the jumping coefficient, it is $u \notin H^2(\Omega)$ with a singularity in the origin of the coordinate system. Consequently, uniform mesh refinement does not yield optimal rates of convergence. Since $f = 0$, it suffices to approximate the solution in $V^k_{h,H}$ with the variational formulation (2.31). Starting from an initial polygonal mesh, see Fig. 5.2 middle, the adaptive BEM-based FEM produces a sequence of locally refined meshes. The approach detects the singularity in the origin of the coordinate system and polygonal elements appear naturally during the local refinement, see Fig. 5.2 right. In Fig. 5.4, the energy error $\|u - u_h\|_b$ as well as the error estimator η_R are plotted with respect to the number of degrees of freedom in logarithmic scale. As expected by the theory the residual based error estimate represents the behaviour of the energy error very well. Furthermore, the adaptive approach yields optimal rates of convergence in the presence of a singularity, namely a slope of $-k/2$ in the logarithmic plot.

Experiment 3: Adaptive Refinement, Closer Look
Using polar coordinates again, let $\Omega = \{\mathbf{x} \in \mathbb{R}^2 : |r| < 1 \text{ and } 0 < \varphi < 3\pi/2\}$ and the boundary data g_D be chosen in such a way that

$$u(r\cos\phi, r\sin\phi) = r^{2/3}\sin\left(\frac{2\phi}{3}\right)$$

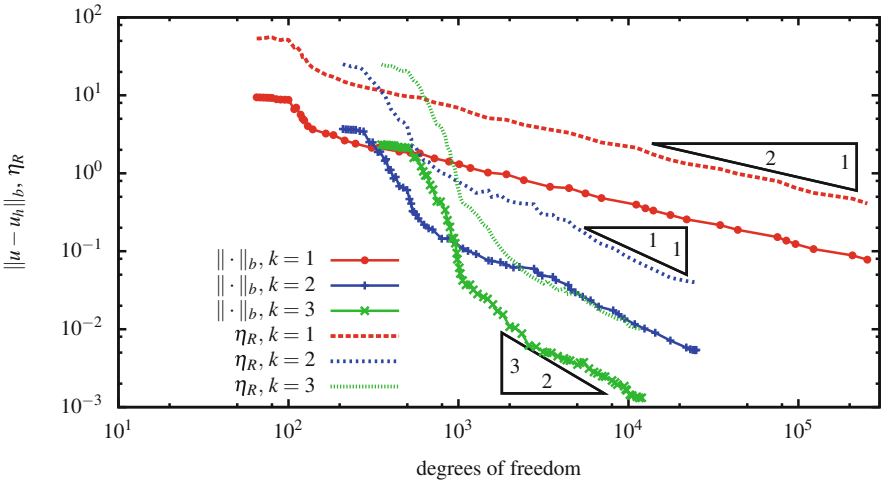

Fig. 5.4 Convergence graph for adaptive mesh refinement with $V_{h,H}^k$, $k = 1, 2, 3$, the energy error and the residual based error estimator are given with respect to the number of degrees of freedom in logarithmic sale

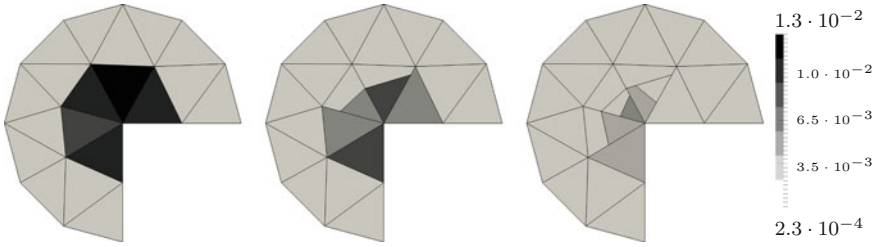

Fig. 5.5 Closer look at the error distribution $|u-u_h|^2_{H^1(K)}$ for the first three meshes in the adaptive refinement approach

is the solution of the boundary value problem

$$-\Delta u = 0 \quad \text{in } \Omega, \qquad u = g_D \quad \text{on } \Gamma.$$

The function u is constructed in such a way that its derivatives have a singularity at the origin of the coordinate system. The boundary value problem is discretized using the first order approximation space V_h^1 and we analyse the first steps in the adaptive refinement strategy in more detail. This will stress the use and the flexibility of polygonal meshes in adaptive computations. For this purpose the error distribution is visualized in Fig. 5.5 for the first three meshes. Each element K is colored according to the value $|u - u_h|^2_{H^1(K)}$. The adaptive algorithm apparently marks and refines the elements with the largest error contribution. The introduced nodes on straight

edges (hanging nodes for classic meshes) are not resolved. Each of these nodes corresponds to a degree of freedom in the finite element computation and thus, improves the approximation within the neighbouring elements. For example, the upper right triangle close to the reentrant corner in Fig. 5.5 is not refined. But, the error reduces due to the additional nodes on the left edge, namely, the triangle became a pentagon in the right most mesh.

Experiment 4: Solution with Strong Internal Layer
Let $\Omega = (0, 1)^2$ and f be chosen such that

$$u(\mathbf{x}) = 16x_1(1 - x_1)x_2(1 - x_2)\arctan(25x_1 - 100x_2 + 50) ,$$

is the exact solution of

$$-\Delta u = f \quad \text{in } \Omega , \qquad u = 0 \quad \text{on } \Gamma .$$

Since u is arbitrary smooth, we expect optimal rates of convergence in the case of uniform mesh refinement in an asymptotic regime. Although the solution u is smooth, it has a strong internal layer along the line $x_2 = 1/2+x_1/4$. The initial mesh is visualized in Fig. 5.6 (left). Furthermore, the first uniform refined mesh is given in the middle of Fig. 5.6. In the right most picture of Fig. 5.6 the adaptively refined mesh for V_h^1 and a relative error of approximately 0.2 is presented. This mesh has been achieved after 19 refinement steps. It is seen that the adaptive strategy refines along the internal layer of the exact solution.

In Fig. 5.7, we give the convergence graphs for the first, second and third order method and for the uniform as well as the adaptive strategy. In all cases we recover the optimal rates of convergence which correspond to a slope of $-k/2$. But, for the uniform refinement, the internal layer has to be resolved sufficiently before the optimal rates are achieved. Since the adaptive strategy resolves the layer

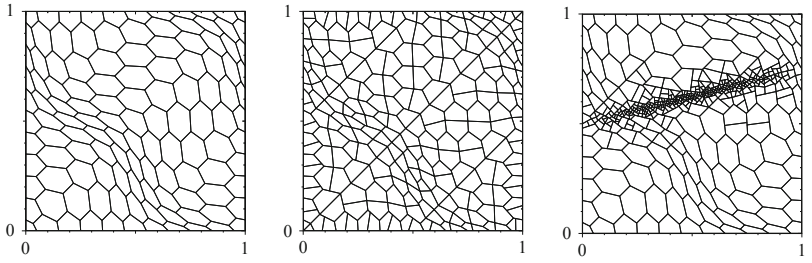

Fig. 5.6 Initial mesh (left), uniformly refined mesh (middle), adaptively refined mesh for $k = 1$ and $\|u - u_h\|_b/\|u\|_b \approx 0.2$ (right) for the solution with an internal layer

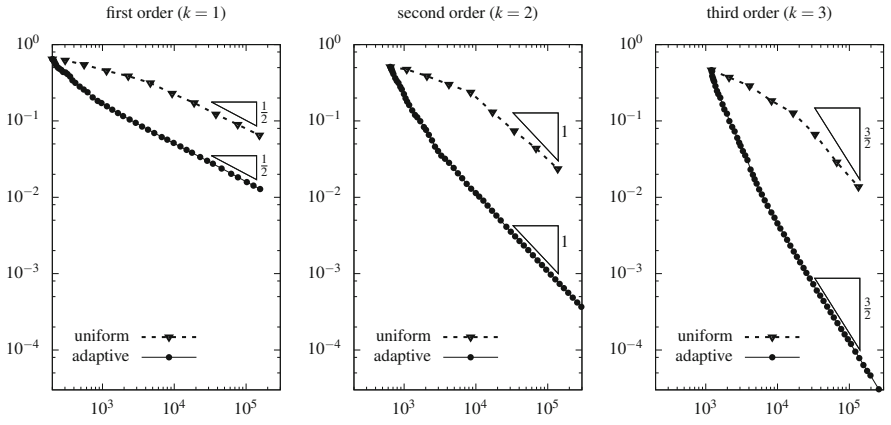

Fig. 5.7 Convergence of the relative energy error $\|u - u_h\|_b / \|u\|_b$ with respect to the number of degrees of freedom for the approximation orders $k = 1, 2, 3$ on uniformly and adaptively refined meshes

automatically, the adaptive BEM-based FEM is much more accurate for the same number of unknowns.

In Chap. 3, we have introduced the notion of anisotropic polytopal meshes. Such meshes are especially suited for the approximation of functions with strong layers. In Sect. 3.4.6, an algorithm has been given in order to adapt the mesh to the layers of a function sought to be approximated. In this algorithm, it has been assumed that the function and its derivatives are known. The anisotropic polytopal meshes clearly outperformed the uniformly and adaptively refined meshes with isotropic elements in that case. In this section, we have investigated an adaptive refinement method that does not need the knowledge of the exact solution and the refinement is done fully automatic. So the next step would be to combine the adaptive algorithm driven by a posteriori error estimates with anisotropic mesh refinement for problems containing strong layers in their solutions.

5.3 Goal-Oriented Error Estimation

In the previous section, the adaptive algorithm has been driven by an error indicator penalizing the error measured in the energy norm. In engineering applications, however, this quantity might not be of importance for the considered simulation. In this case, goal-oriented error estimation techniques are advantages that enable adaptive refinements with different emphases. The dual-weighted residual (DWR) method allows for estimating the error $u - u_h$ between the exact solution of the boundary value problem and its Galerkin approximation in terms of a general (error) functionals J. These functionals can be norms but also more general expressions,

like point-values, (local) averages or other quantities of interest. Error estimators based on the DWR method always consist of residual evaluations, that are weighted by (local) adjoint sensitivity measures. These sensitivities are the solution to adjoint problems that measure the influence of the error functional J. The DWR technique goes back to [21, 22] and is motivated by [74]. Important further developments in the early stages have been accomplished in [3, 4, 18, 37, 83, 134, 137, 141].

In this section, we restrict ourselves to the two-dimensional case $d = 2$ although the approach is applicable in general dimensions. Thus, let $\Omega \subset \mathbb{R}^2$ be a bounded polygonal domain with boundary $\Gamma = \Gamma_D \cup \Gamma_N$ and $|\Gamma_D| > 0$. Furthermore, we only consider the Poisson problem, i.e. $a \equiv 1$,

$$\begin{aligned} -\Delta u &= f \quad && \text{in } \Omega \ , \\ u &= 0 \quad && \text{on } \Gamma_D \ , \\ \nabla u \cdot \mathbf{n} &= g_N \quad && \text{on } \Gamma_N \ , \end{aligned}$$

with source function f, homogeneous Dirichlet condition and Neumann data g_N for simplicity. This setting is sufficient to highlight the key concepts which can be applied to more general problems.

5.3.1 DWR Method for Linear Goal Functionals

The DWR method is aimed to measure the error in an adaptive algorithm via certain quantities of interest, i.e., goal functionals $J(\cdot)$. Although the theory is applicable for non-linear goal functionals, see [22], we restrict ourselves to the linear case. Such quantities of interest can be mean values of the solution and its derivatives or more involved technical values such as drag or lift in fluid dynamics. These examples include, for instance,

$$J(u) = \int_\Omega u \, \mathrm{d}\mathbf{x} \ , \quad J(u) = \int_\Gamma \nabla u \cdot \mathbf{n} \, \mathrm{d}s \ , \quad J(u) = u(\mathbf{x}^*), \ \mathbf{x}^* \in \Omega \ , \tag{5.7}$$

that are a mean value, a line integral related to the stress values in elasticity and a point value. If the exact solution u is unknown and only its approximation by a discrete function u_h is given, the question arises, whether we can bound the error

$$J(u) - J(u_h) \ .$$

The DWR approach tackles this task by exploiting a dual problem

$$\text{Find } z \in H^1_D(\Omega) : \quad b(v, z) = J(v) \quad \forall v \in H^1_D(\Omega) \ , \tag{5.8}$$

where the bilinear form coincides for the Poisson equation with the one in the primal problem. The boundary conditions are of homogeneous Dirichlet and Neumann type. The derivation of the dual (or better 'adjoint') problem follows the Lagrangian formalism that is well-known in optimization. The original motivation is provided in detail in [22]. The solvability and regularity theory for (5.8) follows standard arguments. Thus, we may recognize that the last functional in (5.7), the point evaluation, does not fall into this theory, since it is not defined for functions in $H^1(\Omega)$. Consequently, one may regularize the point evaluation by a convolution with a mollifier, i.e. with an appropriate smooth function having small local support.

Choosing $v = u - u_h$ in (5.8) and applying the Galerkin orthogonality, namely $b(u - u_h, v_h) = 0$ for all $v_h \in V^k_{h,D}$, yields

$$b(u - u_h, z - v_h) = J(u - u_h) \ .$$

This is a key point in the DWR method. Since v_h is an arbitrary discrete test function, we can, for instance, use an interpolation or projection $v_h = \mathfrak{i}_h z$ to obtain an error representation.

Proposition 5.5 *For the Galerkin approximation of the above bilinear form, we have the a posteriori error identity:*

$$J(u - u_h) = b(u - u_h, z - \mathfrak{i}_h z) \ . \tag{5.9}$$

We cannot simply evaluate the error identity because z is only analytically known in very special cases. Consequently, in order to obtain a computable error representation, z is approximated through a discrete function z^*_h, that is, as the primal problem itself, obtained from solving a discretized version of (5.8).

Proposition 5.6 *Let z^*_h be the discrete dual function. For the Galerkin approximation of the above bilinear form, we have the a posteriori error representation*

$$J(u - u_h) \approx b(u - u_h, z^*_h - \mathfrak{i}_h z^*_h) \ .$$

The straight forward choice of $z^*_h = z_h \in V^k_{h,D}$ as solution of

$$b(v_h, z_h) = J(v_h) \quad \forall v_h \in V^k_{h,D}$$

is not applicable. Since $z_h - \mathfrak{i}_h z_h \in V^k_{h,D}$ and due to the Galerkin orthogonality this choice yields

$$J(u - u_h) \approx b(u - u_h, z_h - \mathfrak{i}_h z_h) = 0 \ .$$

For the evaluation of the error in the form (5.9), we have to calculate approximations $z^*_h - \mathfrak{i}_h z^*_h$ of the interpolation errors $z - \mathfrak{i}_h z$. This approximation is the critical part in the DWR framework that limits strict reliability [132]. A remedy is only given by

spending sufficient effort on the estimation of these weights on fine meshes [22, 52] or an additional control of the approximation error in $z - \mathrm{i}_h z$, see [132]. As just mentioned, it is well-known that the discrete approximation of $z - \mathrm{i}_h z$ must be finer than the trial space for the primal variable as the residual is orthogonal on $V_{h,D}^k$. On triangular and quadrilateral meshes there are basically two main strategies in the literature.

- Global more accurate approximation: The dual problem is either treated on the same mesh with a higher order approximation space or on a finer mesh with the same order approximation space. Both variants are quite expensive [22].
- Local more accurate reconstruction: The primal and dual problem are treated on the same mesh with the same approximation space, but, the dual approximation is post-processed locally using a patch-mesh structure [22]. This is a cheaper alternative, but needs an agglomeration of elements.

Both strategies are applicable on polygonal meshes. However, we even propose a new approach which is based on a local post-processing using a single element. This enables the treatment of the primal and dual problem with the same mesh and approximation space followed by an element-wise higher order reconstruction in order to obtain z_h^*. Detailed explanations of this variant are provided in Sect. 5.3.3.2.

In order to obtain an error estimator, the right hand side of (5.9) is either estimated or approximated by some $\eta(u_h, z)$. The quality of this error estimator with respect to the true error is measured in terms of the effectivity index I_{eff} with

$$I_{\text{eff}}(u_h, z) = \left| \frac{\eta(u_h, z)}{J(u - u_h)} \right| \to 1 \quad \text{for } h \to 0 \,. \tag{5.10}$$

In many applications, the asymptotic sharpness 1 cannot be achieved, but it should be emphasized that even overestimations of a factor 2 or 4 still yield a significant reduction of the computational cost in order to obtain a desired accuracy for the goal functional $J(u)$. The residual based error estimator studied in Sect. 5.2 is known to have a bad effectivity. In the numerical experiments in Sect. 5.2.3 the error estimator η_R overestimated the true error by a factor between 5 and 10 in the problem with singular solution and by a factor between 7 and 22 in the problem with smooth solution containing an internal layer. The DWR method produces sharper estimates.

In the following sections, we explain the realization of the dual-weighted residual method for goal-oriented error estimation on polygonal discretizations. We first introduce special meshes and then recall various strategies to discretize the primal and dual problems. In particular, we introduce an element-based post-processing of the dual solution. The above mentioned error estimator $\eta(u_h, z)$ is the basis for the derivation of a posteriori error estimates. In order to use this formulation from Proposition 5.5 for mesh refinement, we need to localize the error contributions on each element. Therefore, two error representations are finally recapitulated: using the classical method with strong forms of the differential operator, and secondly, using a partition of unity for the variational form.

5.3.2 Preparation for Post-processing: Special Meshes

The local post-processing of the dual solution might be done on coarsened meshes obtained by agglomerating polygonal elements in a classical way. However, on these general meshes we might alternatively use novel kinds of hierarchies. In the later described post-processing of the dual solution, we exploit this possibility. Therefore, we do not allow general polygonal meshes $\mathscr{K}_h$ as described in Sect. 2.2. Here, we restrict ourselves to regular and stable meshes $\mathscr{K}_h$ with polygonal elements having an even number of nodes, such that every second node lies on an straight part of the boundary of the element. Furthermore, we assume that by removing these nodes from the mesh we obtain a coarsened polygonal mesh $\mathscr{K}_{2h}$ which is still regular. In Fig. 5.8, we visualize such meshes $\mathscr{K}_h$ in the middle column and their corresponding coarsened meshes $\mathscr{K}_{2h}$ in the left column. Using these meshes we define the approximation spaces V_h^k and V_{2h}^k, respectively.

The condition on the node count for $\mathscr{K}_h$ is not a real restriction. We can always introduce some additional nodes in the mesh to ensure the requirements. This is also done when we refine some given meshes. The middle column of Fig. 5.8 shows a sequence of uniform refined meshes which are used in later numerical experiments in Sect. 5.3.5. In the refinement procedure each element in the mesh $\mathscr{K}_h$ is bisected as described in Sect. 2.2.3. This yields a mesh which does not satisfy the requirement on the node count for each element in general, see Fig. 5.8 right. However, we can ensure the required structure of the mesh by introducing some additional nodes. This can be observed by comparing the refined, but inappropriate mesh, in the right column of Fig. 5.8 with the next mesh in the sequence depicted in the middle column.

5.3.3 Approximation of the Primal and Dual Solution

The primal and dual problems are approximated on polygonal meshes as described in Chap. 2. For this reason, let $\Omega \subset \mathbb{R}^2$ be a bounded polygonal domain meshed into polygonal elements satisfying the regularity and stability assumption and, in most experiments, the requirement on the node count as described above. The primal variable u is approximated by $u_h \in V_h^k$, which is given by the decoupled weak formulation (2.31) as well as (2.32) and reads in this setting for $u_h = u_{h,H} + u_{h,B}$ with $u_{h,H} \in V_{h,H}^k$ and $u_{h,B} \in V_{h,B}^k$:

$$\begin{aligned} &\text{Find } u_{h,H} \in V_{h,H,D}^k : \\ &b(u_{h,H}, v_h) = (f, v_h)_{L_2(\Omega)} + (g_N, v_h)_{L_2(\Gamma_N)} \quad \forall v_h \in V_{h,H,D}^k , \end{aligned} \tag{5.11}$$

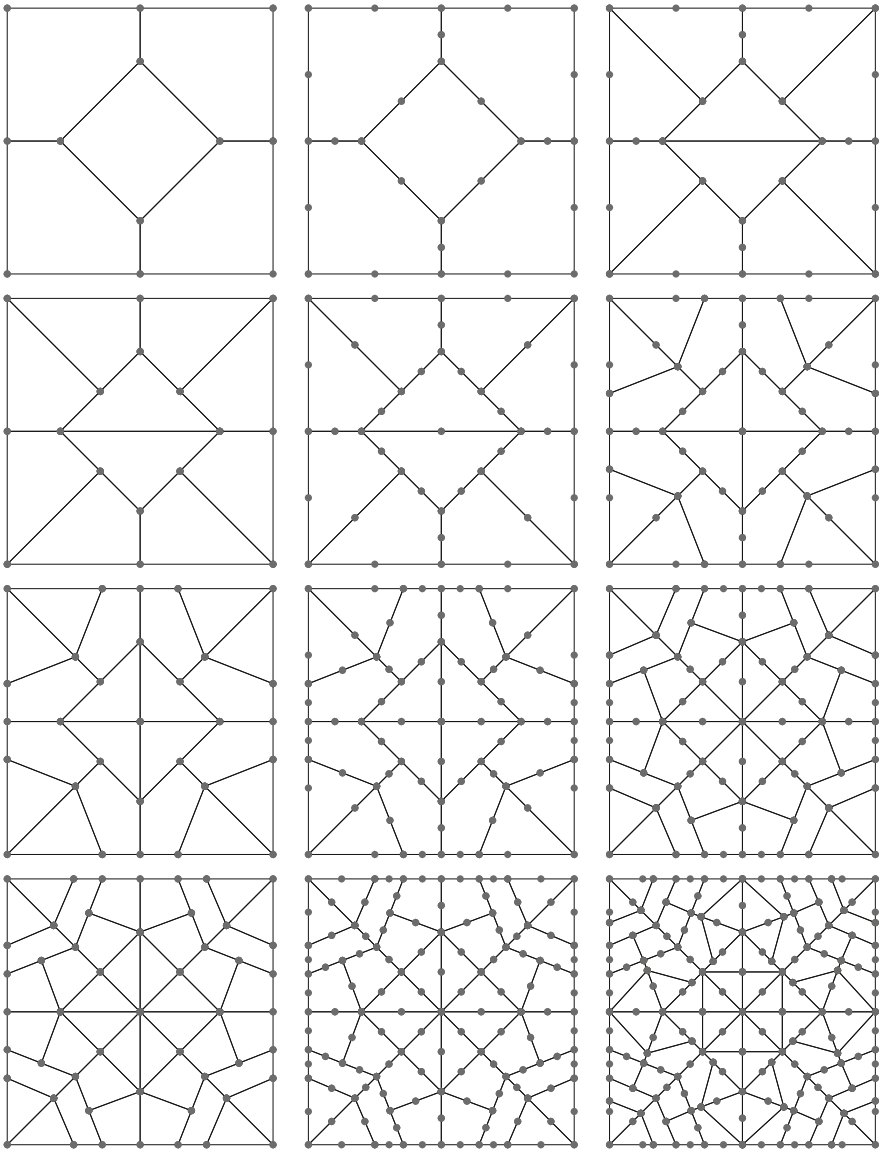

Fig. 5.8 Each row corresponds to the mesh in one FEM simulation, the middle column corresponds to the actual mesh $\mathscr{K}_h$, the left column shows the mesh $\mathscr{K}_{2h}$ after coarsening and the right column shows the mesh after refinement before the nodes are added to ensure the condition on the node count

and

$$\text{Find } u_{h,B} \in V_{h,B}^k : \quad b(u_{h,B}, v_h) = (f, v_h)_{L_2(\Omega)} \quad \forall v_h \in V_{h,B}^k \,. \tag{5.12}$$

For the approximation of the dual solution z we have a corresponding decoupling and we focus on two strategies. Either we use globally a higher order for the approximation, which is, however, practically expensive, or we apply a local post-processing to $z_h \in V_h^k$. The local post-processing is especially attractive for the approximation space of the BEM-based FEM, since there is no need for local agglomerations of elements as we see in the next sections.

5.3.3.1 Dual Solution with Globally Higher Order Discretization

A brute-force strategy to obtain an approximation of the dual solution, which is suited for error estimation, is to solve the discrete variational formulation with higher accuracy. To track the approximation order, we write $u_h = u_h^{(k)} \in V_h^k$ for the approximation of the primal solution. The dual solution can be approximated by $z_h^{(k+1)} \in V_h^{k+1}$ on the same mesh. The choice $z_h^* = z_h^{(k+1)}$ is applicable for the error representation, cf. (5.9). Here, we do not need the restriction on the node count for the mesh $\mathscr{K}_h$. As we already mentioned, this strategy is computationally expensive in practical applications. However, it serves as a good starting point to verify the performance of the dual-weighted residual method on polygonal meshes.

5.3.3.2 Dual Solution Exploiting Local Post-Processing

A more convenient and efficient strategy is to approximate the dual solution by $z_h = z_h^{(k)} \in V_h^k$ on the same mesh with the same approximation order as the primal solution. Afterwards z_h^* is chosen as a post-processed version of z_h on a coarsened mesh with higher approximation order. This strategy is well discussed in the literature for simplicial meshes, see [143] and the references therein. In fact, this has already been introduced in the early studies [22]. The key point is, how the meshes, and especially the coarse meshes, are chosen. Since polygonal meshes are very flexible and inexpensive for coarsening and refining, they are well suited for this task. It is possible to just agglomerate two or more neighbouring elements to construct a coarsened mesh and to proceed in a classical way for the local post-processing.

In the following we describe a slightly different strategy that does not need the agglomeration of elements and is applicable on single elements. We use the meshes $\mathscr{K}_h$ and $\mathscr{K}_{2h}$ discussed in Sect. 5.3.2 satisfying the requirement on the node count. The approach relies on two key ingredients: the hierarchy of the discretization of the element boundaries ∂K in these two meshes and the decoupling of the dual problem analogously to (5.11) and (5.12) for the primal problem.

Let $z_h \in V_h^k$ be the approximation of the dual problem over the mesh $\mathscr{K}_h$. We construct $z_h^* \in V_{2h}^{k+1}$ as locally post-processed function over the mesh $\mathscr{K}_{2h}$. We write the mapping $z_h = z_h^{(k)} \mapsto z_h^* \in V_{2h}^{k+1}$ also in operator notation with $\mathfrak{P}_{2h}^{k+1} : V_h^k \to V_{2h}^{k+1}$ such that $z_h^* = \mathfrak{P}_{2h}^{k+1} z_h^{(k)}$. It is sufficient to define the post-processing on a single element $K \in \mathscr{K}_h$, since it directly generalizes to the entire mesh. By construction, each element $K = K_h \in \mathscr{K}_h$ has a corresponding element $K_{2h} \in \mathscr{K}_{2h}$, which is obtained by skipping every second node on the boundary ∂K_h. Thus, the shapes of these elements coincide and they only differ in the number of nodes on the boundary. Consequently, ∂K_h can be interpreted as a refinement of ∂K_{2h}, or in other words, ∂K_h and ∂K_{2h} are one-dimensional patched meshes of the element boundary. Therefore, it is $\mathscr{P}_{\mathrm{pw}}^k(\partial K_{2h}) \subset \mathscr{P}_{\mathrm{pw}}^k(\partial K_h)$. In terms of the approximation space we set $V_{2h}^k(K_h) = V_h^k(K_{2h}) \subset V_h^k(K_h)$. Since it is clear from the approximation space which element is meant, we skip the index h and $2h$ again.

Suppose we would approximate the dual problem globally in V_{2h}^{k+1}. Then, the weak formulation decouples into a global system of linear equations in order to compute the expansion coefficients of the harmonic basis functions and into a projection of the error functional into the space of element bubble functions. We similarly proceed with the post-processing. Exploiting the hierarchy of the boundary, we construct $z_h^* = z_{h,H}^* + z_{h,B}^* \in V_{2h}^{k+1}(K) = V_{2h,H}^{k+1}(K) \oplus V_{2h,B}^{k+1}(K)$ from the approximation $z_h = z_{h,H} + z_{h,B} \in V_h^k(K)$ in the following way: We set

$$z_{h,H}^* \in V_{2h,H}^{k+1}(K) \text{ as interpolation of } z_{h,H} \in V_{h,H}^k(K) \tag{5.13}$$

and

$$z_{h,B}^* \in V_{2h,B}^{k+1}(K) \text{ as solution of: } \quad (\nabla z_{h,B}^*, \nabla \varphi)_{L_2(K)} = J(\varphi) \quad \forall \varphi \in V_{2h,B}^{k+1}(K) \,. \tag{5.14}$$

The interpolation process in (5.13) is equivalent to an interpolation of a function in $\mathscr{P}_{\mathrm{pw}}^k(\partial K_h)$ by a function in $\mathscr{P}_{\mathrm{pw}}^{k+1}(\partial K_{2h})$. Thus, a standard point-wise interpolation procedure is applied. The definition of $z_{h,B}^*$ is exactly the projection of the error functional into the space of element bubble functions. Both operations are local over a single element and are thus suited for a computationally inexpensive post-processing.

Remark 5.7 The first idea might be to use the interpolation operator $\mathfrak{I}_h^k$ studied in Sect. 2.4 and to set $z_h^* = \mathfrak{I}_{2h}^{k+1} z_h^{(k)}$. But, this strategy does not work. The interpolation affecting the harmonic basis functions yields the same results as described above. However, the transition from the lower order element bubble functions to the higher order ones is not well suited. Since there is no agglomeration of elements and the process is kept on a single element, there is no additional information in the interpolation using higher order element bubble functions. This is reflected by the fact that $V_{h,B}^k(K) = V_{2h,B}^k(K)$. The choice (5.14) overcomes this deficit and includes the required information for the element bubble functions by exploiting the dual problem.

5.3.4 The Localized Error Estimators

In this section, we discuss the localization of the error representation derived in Sect. 5.3.1 on polygonal meshes. The representation involves the adjoint sensitivity measure $z - \mathfrak{i}_h z$ with $\mathfrak{i}_h : V \to V_h^k$. Since the dual solution is not known in general, it is approximated in the numerical tests as discussed in Sect. 5.3.3. In the realization, we replace z in the error estimates by z_h^*. The operator $\mathfrak{i}_h$ is realized in the following with the help of the interpolation operator $\mathfrak{I}_h^k$, which is given and studied in Sect. 2.4.

5.3.4.1 The Classical Way of Localization

The error identity in Proposition 5.5 is realized in the classical way by using the concrete problem, followed by integration by parts on every mesh element $K \in \mathscr{K}_h$, yielding

$$J(u-u_h) = \sum_{K\in\mathscr{K}_h} \Big(\big(f + \Delta u_h, z - \mathfrak{i}_h z\big)_{L_2(K)} - \big(\gamma_1^K u_h, (z - \mathfrak{i}_h z)\big)_{L_2(\partial K)} \Big) + \big(g_N, (z - \mathfrak{i}_h z)\big)_{L_2(\Gamma_N)} .$$

Following the usual procedure for residual based error estimators as in Sect. 5.2.1, we combine each two boundary integrals over element edges to a normal jump and proceed with the Cauchy–Schwarz inequality to derive an upper bound of the error.

Proposition 5.8 *For the BEM-based FEM approximation of the Poisson equation, we have the a posteriori error estimate based on the classical localization:*

$$|J(u-u_h)| \le \eta^{\mathrm{CL}} = \sum_{K\in\mathscr{K}_h} \eta_K^{\mathrm{CL}} \tag{5.15}$$

with

$$\eta_K^{\mathrm{CL}} = \|R_K\|_{L_2(K)} \, \|z - \mathfrak{i}_h z\|_{L_2(K)} + \sum_{E\in\mathscr{E}(K)} \|R_E\|_{L_2(E)} \, \|z - \mathfrak{i}_h z\|_{L_2(E)} , \tag{5.16}$$

where R_K and R_E are the element and edge residuals defined in Sect. 5.2, namely

$$R_K = f + \Delta u_h \quad \text{for } K \in \mathscr{K}_h ,$$

and

$$R_E = \begin{cases} 0 & \text{for } E \in \mathscr{E}_{h,D} , \\ g_N - \gamma_1^K u_h & \text{for } E \in \mathscr{E}_{h,N} \text{ with } E \in \mathscr{E}(K) , \\ -\frac{1}{2}[\![u_h]\!]_E & \text{for } E \in \mathscr{E}_{h,\Omega} . \end{cases}$$

According to the definition of the trial space we have $\Delta u_h \in \mathscr{P}^{k-2}(K)$ in each $K \in \mathscr{K}_h$. Since most of the basis functions are harmonic, Δu_h is directly obtained by the expansion coefficients of u_h corresponding to the element bubble functions. The term $\gamma_1^K u_h$ is treated by means of boundary element methods in the realization and therefore it is approximated in $\mathscr{P}^{k-1}_{\mathrm{pw,d}}(\partial K)$.

The local error indicator (5.16) is usually estimated in order to separate it into two parts such that $\eta_K^{\mathrm{CL}} \le \mathfrak{r}_K(u_h)\mathfrak{w}_K(z)$, see, e.g., [4, 18, 21, 22, 143]. The first part $\mathfrak{r}_K(u_h)$ contains the residual with the discrete solution u_h and the problem data and the second part $\mathfrak{w}_K(z)$ contains the adjoint sensitivity measure $z - \mathfrak{i}_h z$. The separation is obtained by further applications of the Cauchy–Schwarz inequality and reads in our notation

$$|J(u-u_h)| \le \sum_{K\in\mathscr{K}_h} \underbrace{\left(\|R_K\|_{L_2(K)} + h_K^{-1/2}\|R_E\|_{L_2(\partial K)}\right)}_{=\mathfrak{r}_K(u_h)} \cdot \underbrace{\left(\|z-\mathfrak{i}_h z\|_{L_2(K)} + h_K^{1/2}\|z-\mathfrak{i}_h z\|_{L_2(\partial K)}\right)}_{=\mathfrak{w}_K(z)} . \tag{5.17}$$

In order to incorporate the polygonal structure of the elements and in particular the different numbers and lengths of their edges, we propose to split the L_2-norms over the boundaries of the elements. This refined manipulation yields

$$|J(u-u_h)| \le \sum_{K\in\mathscr{K}_h} \underbrace{\left(\|R_K\|^2_{L_2(K)} + \sum_{E\in\mathscr{E}(K)} h_E^{-1}\|R_E\|^2_{L_2(E)}\right)^{1/2}}_{=\mathfrak{r}_K(u_h)} \cdot \underbrace{\left(\|z-\mathfrak{i}_h z\|^2_{L_2(K)} + \sum_{E\in\mathscr{E}(K)} h_E\|z-\mathfrak{i}_h z\|^2_{L_2(E)}\right)^{1/2}}_{=\mathfrak{w}_K(z)} . \tag{5.18}$$

The powers of h_K and h_E in (5.17) and (5.18) are chosen in such a way that the volume and boundary terms contribute in the right proportion. This weighting of the norms implicitly makes use of $h_E \sim h_K$, which is guaranteed by the stability of the polygonal meshes. For triangular and quadrilateral meshes the terms h_E and h_K only differ by a small multiplicative factor. (For quadrilaterals it is $h_K = \sqrt{2}h_E$.) In polygonal meshes, however, the ratio $h_K/h_E < c_{\mathscr{K}}$ can be large and it might even blow up in the numerical tests, if the stability is not enforced. Due to these reasons, it seems to be natural to weight directly the volume term $\|R_K\|_{L_2(K)}$ with $\|z-\mathfrak{i}_h z\|_{L_2(K)}$ and the edge term $\|R_E\|_{L_2(E)}$ with $\|(z-\mathfrak{i}_h z)\|_{L_2(E)}$ which gives rise to Proposition 5.8.

5.3.4.2 A Variational Error Estimator with PU Localization

We use a new localization approach [143] based on the variational formulation. Localization is simply based on introducing a partition of unity (PU) into the global error representation Proposition 5.5. In the case of triangular or quadrilateral meshes, the (bi-)linear basis functions are usually utilized, which are associated with nodes. The same is possible for polygonal meshes and the corresponding nodal basis functions, cf. Sect. 2.3.1, which satisfy the partition of unity property. However, this yields a node-wise error indicator, whereas the adaptive refinement is an element-wise procedure. Therefore, we define an element-wise partition of unity in order to obtain directly an element-wise indicator. For this reason, let $\mathfrak{n}(\mathbf{z}) = |\{K \in \mathscr{K}_h : \mathbf{z} \in \mathscr{N}(K)\}|$ be the number of neighbouring elements to the node $\mathbf{z} \in \mathscr{N}_h$. We can write

$$1 = \sum_{\mathbf{z}\in\mathscr{N}_h} \psi_{\mathbf{z}} = \sum_{K\in\mathscr{K}_h} \sum_{\mathbf{z}\in\mathscr{N}(K)} \frac{1}{\mathfrak{n}(\mathbf{z})}\psi_{\mathbf{z}} = \sum_{K\in\mathscr{K}_h} \chi_K \quad \text{on } \Omega \ ,$$

and thus obtain a new partition of unity employing the element-wise functions

$$\chi_K = \sum_{\mathbf{z}\in\mathscr{N}(K)} \frac{1}{\mathfrak{n}(\mathbf{z})}\psi_{\mathbf{z}} \ . \tag{5.19}$$

The support of χ_K is local and covers the neighbouring elements of K, namely

$$\operatorname{supp}\chi_K = \overline{\{\mathbf{x}\in K' : \ K' \in \mathscr{K}_h, \overline{K}\cap\overline{K'} \neq \varnothing\}} = \overline{\omega}_K \ .$$

Inserting the partition of unity into the global error representation Proposition 5.5 yields

$$J(u-u_h) = \sum_{K\in\mathscr{K}_h} b\big(u-u_h, (z-\mathfrak{i}_h z)\chi_K\big) \ .$$

Consequently, when we refer from now on to the PU-based localization technique, we mean the following error representation.

Proposition 5.9 *For the BEM-based FEM approximation of the Poisson equation, we have the element-wise PU-DWR a posteriori error representation and estimate*

$$J(u-u_h) = \eta^{\mathrm{PU}} = \sum_{K\in\mathscr{K}_h} \eta_K^{\mathrm{PU}} \quad \textit{and} \quad |J(u-u_h)| \le \eta_{\mathrm{abs}}^{\mathrm{PU}} = \sum_{K\in\mathscr{K}_h} |\eta_K^{\mathrm{PU}}| \ , \tag{5.20}$$

respectively, with

$$\eta_K^{\mathrm{PU}} = \big(f, (z-\mathfrak{i}_h z)\chi_K\big)_{L_2(\Omega)} + \big(g_N, (z-\mathfrak{i}_h z)\chi_K\big)_{L_2(\Gamma_N)} - \big(\nabla u_h, \nabla((z-\mathfrak{i}_h z)\chi_K)\big)_{L_2(\Omega)} \ .$$

We finish this section by a comment on the practical realization. Even if high-order approximations are used for the primal and dual problems, the PU can be realized using a lowest order method involving the nodal basis functions only.

5.3.5 Numerical Tests

In this section, we substantiate our formulations of the dual-weighted residual estimator and the treatment of the dual solution with several different numerical tests and various goal functionals. In the first example, we consider the standard Poisson problem with a regular goal functional. The second example considers a norm-based goal functional. In the third example we study adaptivity in detail. In all examples, we compare the classical and PU localization techniques. Moreover, we compare as previously mentioned different ways to approximate the dual solution.

In analyzing our results, we notice that the tables and graphs are given with respect to the number of degrees of freedom (DoF) in the following. This highlights the fact that the considered sequences of meshes may have the same shapes of elements, but have different numbers of degrees of freedom. This behaviour is due to the mesh requirement for the local post-processing involving additional nodes on the boundaries of the elements. The degrees of freedom are also the usual criterion for adaptive refined meshes.

The adaptive algorithm discussed in Sect. 5.1 has been realized in a slightly adjusted way. In the **SOLVE** step, we additionally have to compute the approximate (higher order) dual solution z_h^*. For the error estimator we now distinguish between $\eta = \sum_K \eta_K$ and $\eta_{\text{abs}} = \sum_K |\eta_K|$ in **ESTIMATE**. Note that $\eta_{\text{abs}}^{\text{CL}} = \eta^{\text{CL}}$ but $\eta_{\text{abs}}^{\text{PU}} \neq \eta^{\text{PU}}$. This also influences the formulation in the marking later on since the error indicators are not squared here. In the **MARK** step, we utilize this time the equidistribution strategy such that all elements K are marked that have values $|\eta_K|$ above the average $\theta \eta_{\text{abs}}/|\mathscr{K}_h|$. Furthermore, we point out that not all theoretical assumptions on the regularity and stability of the mesh from Sect. 2.2 are enforced in **REFINE** for the following tests. During the refinement, the edge lengths may degenerate with respect to the element diameter. If not otherwise stated, all appearing volume integrals are treated by numerical quadrature over polygonal elements as described in Sect. 4.5.1.

Problem 1: Verification in Terms of a Domain Goal Functional
Let $\Omega = (0, 1)^2$. We consider the boundary value problem

$$-\Delta u = 1 \quad \text{in } \Omega\,, \qquad u = 0 \quad \text{on } \Gamma\,,$$

on two uniform sequences of meshes depicted in Fig. 5.8 (left and middle columns). With a little abuse of notation we denote the sequence of meshes by $\mathscr{K}_{2h}$ and $\mathscr{K}_h$ for

the left and middle column in Fig. 5.8, respectively. The goal functional is chosen as

$$J(v) = \int_{\Omega} v \, \mathrm{d}\mathbf{x} \,,$$

such that the dual and primal problems coincide. The regularity of the solutions is only limited by the corners of the domain and consequently, it is $u, z \in H^{3-\varepsilon}(\Omega)$ for arbitrary small $\varepsilon > 0$. We use the reference value $J(u) \approx 0.03514425375 \pm 10^{-10}$ taken from [143] for the convergence analysis.

In the first experiment, we compare the different representations of the classical localization technique given in Sect. 5.3.4.1. Here we detect a significant difference depending on the partition into residual terms and dual weights of the classical estimator. The primal solution is approximated in V_h^1 and the dual solution is treated by globally higher order, i.e. $z_h^* = z_h^{(2)}$. For this choice, we do not need the requirement on the node count for the meshes. Therefore, we perform the computations on the mesh sequence $\mathscr{K}_{2h}$ of the unite square Ω. The effectivity index I_{eff} is presented in Table 5.1. For comparisons, we also provide results computed on a sequence of structured meshes with rectangular elements. Obviously, the sharpened estimate (5.18) performs better than the usual form (5.17) of the estimator. We observe, however, that the effectivity index is indeed closest to one for the estimate (5.15) which does not separate the residual part from the sensitivity measure. Therefore, we only apply (5.15) in the following experiments for the classical localization. Furthermore, the comparison with structured meshes indicate that the polygonal shapes of the elements do not influence the effectivity on these uniform refined meshes.

Next, we compare the effectivity index for the PU-based and the classical localization with (5.15). The problems are approximated with $k = 1, 2$. In Table 5.2, we show I_{eff} for the choice $z_h^* = z_h^{(k+1)}$ on a sequence of meshes $\mathscr{K}_{2h}$. The

Table 5.1 Problem 1 approximated with $u_h \in V_h^1$, and dual solution treated by globally higher order, i.e. $z_h^* = z_h^{(2)}$; comparison of effectivity for different representations of the classic localization on a mesh sequence $\mathscr{K}_{2h}$ and on structured meshes

Polygonal-meshes					Quad-meshes		
DoF	$J(u - u_h^{(1)})$	$I_{\text{eff}}^{\text{CL}}$ (5.15)	$I_{\text{eff}}^{\text{CL}}$ (5.17)	$I_{\text{eff}}^{\text{CL}}$ (5.18)	DoF	$J(u - u_h^{(1)})$	$I_{\text{eff}}^{\text{CL}}$ (5.15)
4	5.52×10^{-3}	3.01	6.30	3.31	9	2.56×10^{-3}	2.91
8	3.48×10^{-3}	2.21	6.56	4.03	49	6.51×10^{-4}	2.93
13	4.30×10^{-3}	1.74	4.83	2.59	121	2.90×10^{-4}	2.93
25	2.33×10^{-3}	2.02	5.42	2.98	225	1.64×10^{-4}	2.92
57	1.32×10^{-3}	1.99	5.89	3.37	361	1.05×10^{-4}	2.92
129	5.36×10^{-4}	2.29	6.47	3.64	529	7.27×10^{-5}	2.92
289	2.63×10^{-4}	2.34	6.73	3.84	729	5.35×10^{-5}	2.92
620	1.17×10^{-4}	2.65	7.45	4.28	961	4.09×10^{-5}	2.92
1297	5.67×10^{-5}	2.66	7.48	4.24	1225	3.23×10^{-5}	2.92

Table 5.2 Problem 1 approximated with $u_h \in V_h^k$, $k = 1, 2$ and dual solution treated by globally higher order, i.e. $z_h^* = z_h^{(k+1)}$; comparison of effectivity for PU localization and classical localization with (5.15) on mesh sequence $\mathscr{K}_{2h}$

DoF	$J\left(u - u_h^{(1)}\right)$	$I_{\text{eff}}^{\text{CL}}$ (5.15)	$I_{\text{eff}}^{\text{PU}}$	DoF	$J\left(u - u_h^{(2)}\right)$	$I_{\text{eff}}^{\text{CL}}$ (5.15)	$I_{\text{eff}}^{\text{PU}}$
8	3.48×10^{-3}	2.21	1.16	35	1.76×10^{-4}	2.09	1.30
13	4.30×10^{-3}	1.74	0.99	65	7.36×10^{-5}	1.59	1.24
25	2.33×10^{-3}	2.02	1.00	129	1.41×10^{-5}	1.65	1.30
57	1.32×10^{-3}	1.99	1.01	273	4.00×10^{-6}	1.60	1.27
129	5.36×10^{-4}	2.29	1.03	577	7.80×10^{-7}	1.68	1.34
289	2.63×10^{-4}	2.34	1.04	1217	1.93×10^{-7}	1.66	1.34
620	1.17×10^{-4}	2.65	1.07	2519	3.63×10^{-8}	1.80	1.41
1297	5.67×10^{-5}	2.66	1.07	5153	4.95×10^{-9}	3.62	2.90

Table 5.3 Problem 1 approximated with $u_h \in V_h^k$, $k = 1, 2$ and dual solution treated by local post-processing, i.e. $z_h^* = \mathfrak{P}_{2h}^{k+1} z_h^{(k)}$; comparison of effectivity for classical with (5.15) and PU localization on mesh sequence $\mathscr{K}_h$

DoF	$J\left(u - u_h^{(1)}\right)$	$I_{\text{eff}}^{\text{CL}}$ (5.15)	$I_{\text{eff}}^{\text{PU}}$	DoF	$J\left(u - u_h^{(2)}\right)$	$I_{\text{eff}}^{\text{CL}}$ (5.15)	$I_{\text{eff}}^{\text{PU}}$
25	3.41×10^{-3}	1.40	0.92	69	1.21×10^{-5}	1.20	0.57
45	1.76×10^{-3}	1.96	0.96	129	1.07×10^{-5}	1.27	0.86
89	9.17×10^{-4}	2.05	0.95	257	8.69×10^{-7}	1.19	0.68
193	4.63×10^{-4}	2.36	0.96	545	6.76×10^{-7}	1.50	1.08
465	2.31×10^{-4}	1.99	0.93	1249	4.36×10^{-8}	1.34	0.79
953	1.14×10^{-4}	2.10	0.95	2545	2.65×10^{-8}	1.56	1.14
2069	5.66×10^{-5}	2.12	0.95	5417	1.50×10^{-9}	2.01	1.39
4269	2.83×10^{-5}	2.09	0.96	11,097	$<10^{-9}$	–	–

effectivity index for the PU localization is close to one whereas the classical localization lacks on effectivity for the first order approximation $k = 1$. For $k = 2$ the effectivity I_{eff}^{CL} is improved.

Furthermore, in Table 5.3, we applied the local post-processing of $z_h^{(k)}$ in order to construct $z_h^* = \mathfrak{P}_{2h}^{k+1} z_h^{(k)}$ and therefore the computations are done on the sequence of meshes $\mathscr{K}_h$, which satisfy the condition on the node count. Although the elements have the same shapes in the sequences of meshes, the number of degrees of freedom is larger in $\mathscr{K}_h$ than in $\mathscr{K}_{2h}$. Both localization strategies show good effectivity in Table 5.3. Due to the local post-processing instead of the globally higher order approximation for the dual solution, the computational cost is significantly reduced compared to the experiments for Table 5.2. We finally remark that for obtaining errors of similar order in the case of $k = 2$, the meshes in Table 5.2 are one times more refined in comparison to the method presented in Table 5.3. However, as just explained, the mesh itself is coarser but the number of degrees of freedom is higher on the other hand when using the local post-processing of $z_h^{(k)}$.

Problem 2: A Norm-Based Goal Functional
In our second example, let again $\Omega = (0,1)^2$. We consider the boundary value problem

$$-\Delta u = f \quad \text{in } \Omega\,, \qquad u = 0 \quad \text{on } \Gamma\,,$$

where f is chosen such that $u(\mathbf{x}) = \sin(\pi x_1)\sin(\pi x_2)$ is the analytical solution. As in the previous problem, we compare the different localization techniques and the two choices of z_h^*. The computations are done solely on the sequence of meshes satisfying the node count condition, which is depicted in Fig. 5.8 in the middle column. The error functional is chosen as

$$J(v) = \frac{(u-u_h, v)_{L_2(\Omega)}}{\|u-u_h\|_{L_2(\Omega)}}\,,$$

such that $J(u-u_h) = \|u-u_h\|_{L_2(\Omega)}$. Our results of the effectivity indices are shown in the Tables 5.4 and 5.5. All indices are close to one and behave similar to those of the previous Problem 1. I_{eff}^{PU} is hardly effected by the different approximations of the dual solution and also the classical localization shows comparable effectivity. Consequently, the computationally less expensive post-processing is to favor over the higher order approximation of the dual solution in practical applications.

Problem 3: Adaptivity
Finally, let $\Omega = (-1,1)\times(-1,1)\setminus[0,1]\times[-1,0]$ be an L-shaped domain and its boundary is split into $\Gamma_D = \{(x_1,x_2)\in\mathbb{R}^2 : x_1\in[0,1],\ x_2 = 0 \text{ or } x_1 = 0,\ x_2\in[-1,0]\}$ and $\Gamma_N = \partial\Omega\setminus\Gamma_D$. We consider the mixed boundary value problem

$$-\Delta u = 0 \quad \text{in } \Omega\,, \qquad u = 0 \quad \text{on } \Gamma_D\,, \qquad \nabla u\cdot\mathbf{n} = g_N \quad \text{on } \Gamma_N\,,$$

Table 5.4 Problem 2 approximated with $u_h \in V_h^k$, $k = 1,2$ and dual solution treated by globally higher order, i.e. $z_h^* = z_h^{(k+1)}$; comparison of effectivity for PU localization and classical localization with (5.15) on mesh sequence $\mathscr{K}_h$

DoF	$J\left(u-u_h^{(1)}\right)$	$I_{\text{eff}}^{\text{CL}}$ (5.15)	$I_{\text{eff}}^{\text{PU}}$	DoF	$J\left(u-u_h^{(2)}\right)$	$I_{\text{eff}}^{\text{CL}}$ (5.15)	$I_{\text{eff}}^{\text{PU}}$
25	3.80×10^{-2}	1.76	0.92	69	5.64×10^{-3}	1.38	0.95
45	2.10×10^{-2}	1.99	0.98	129	2.90×10^{-3}	1.26	0.95
89	1.05×10^{-2}	1.91	0.81	257	8.48×10^{-4}	1.27	0.97
193	5.34×10^{-3}	2.05	0.83	545	3.57×10^{-4}	1.29	0.96
465	2.59×10^{-3}	1.98	0.82	1249	1.17×10^{-4}	1.46	0.93
953	1.35×10^{-3}	2.06	0.83	2545	4.04×10^{-5}	1.35	0.98
2069	6.75×10^{-4}	2.11	0.82	5417	1.59×10^{-5}	1.37	0.99
4269	3.38×10^{-4}	2.04	0.84	11,097	5.26×10^{-6}	1.36	1.05

Table 5.5 Problem 2 approximated with $u_h \in V_h^k$, $k = 1, 2$ and dual solution treated by local post-processing, i.e. $z_h^* = \mathfrak{P}_{2h}^{k+1} z_h^{(k)}$; comparison of effectivity for classical with (5.15) and PU localization on mesh sequence $\mathscr{K}_h$

DoF	$J\left(u - u_h^{(1)}\right)$	$I_{\text{eff}}^{\text{CL}}$ (5.15)	$I_{\text{eff}}^{\text{PU}}$	DoF	$J\left(u - u_h^{(2)}\right)$	$I_{\text{eff}}^{\text{CL}}$ (5.15)	$I_{\text{eff}}^{\text{PU}}$
25	3.80×10^{-2}	1.65	0.83	69	5.64×10^{-3}	1.26	0.95
45	2.10×10^{-2}	1.79	0.86	129	2.90×10^{-3}	1.28	0.96
89	1.05×10^{-2}	2.29	0.84	257	8.48×10^{-4}	1.28	0.97
193	5.34×10^{-3}	2.16	0.80	545	3.57×10^{-4}	1.30	0.95
465	2.59×10^{-3}	2.24	0.82	1249	1.17×10^{-4}	1.29	0.89
953	1.35×10^{-3}	2.20	0.82	2545	4.04×10^{-5}	1.32	0.97
2069	6.75×10^{-4}	2.25	0.82	5417	1.59×10^{-5}	1.33	0.97
4269	3.38×10^{-4}	2.19	0.82	11,097	5.26×10^{-6}	1.34	1.01

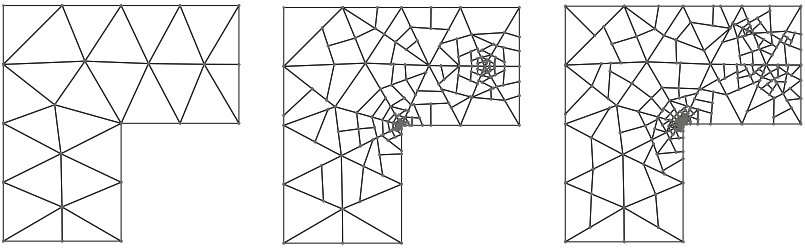

Fig. 5.9 Initial mesh of the L-shaped domain in Problem 3 with triangular elements (left) and adaptive meshes for $k = 2$ after 10 refinements for classical (middle) and PU (right) localization, where the dual problem is treated by globally higher order, i.e. $z_h^* = z_h^{(k+1)}$

where g_N is chosen with the help of polar coordinates (r, ϕ), such that

$$u(r\cos\phi, r\sin\phi) = r^{2/3}\sin\left(\tfrac{2}{3}\phi\right)$$

is the exact solution. This is a classical problem for mesh adaptivity, since the gradient of the solution inherits a singularity at the reentrant corner in the origin of the coordinate system. It holds $u \in H^{5/3}(\Omega)$. The considered goal functional is a point evaluation

$$J(v) = v(\mathbf{x}^*)\,,$$

where $\mathbf{x}^*$ is chosen as the upper right node inside the domain, which is adjacent to six elements of the initial mesh, see Fig. 5.9 (left). We apply the adaptive strategy and compare the resulting meshes for the different localization techniques and approximations of the dual solution.

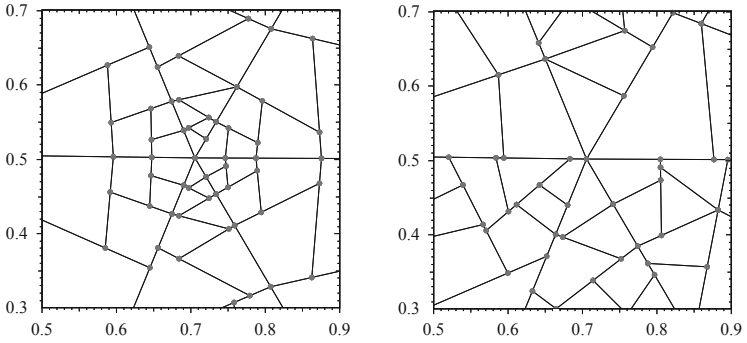

Fig. 5.10 Zoom into L-shaped domain in Problem 3 with adaptive meshes for $k = 2$ after 10 refinements for classical (left) and PU (right) localization, where the dual problem is treated by globally higher order, i.e. $z_h^* = z_h^{(k+1)}$

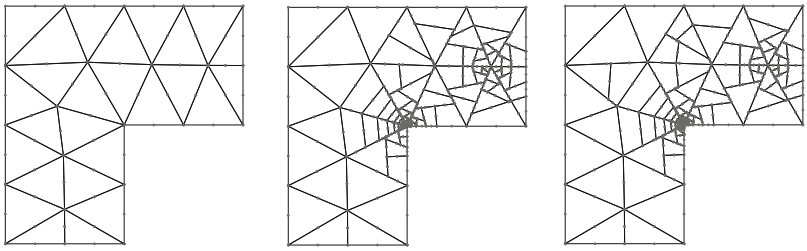

Fig. 5.11 Initial mesh of the L-shaped domain in Problem 3 with triangular elements (left), which are actually degenerated hexagons, and adaptive meshes for $k = 2$ after 10 refinements for classical (middle) and PU (right) localization, where the dual problem is treated by local post-processing, i.e. $z_h^* = \mathfrak{P}_{2h}^{k+1} z_h^{(k)}$

In Fig. 5.9, we display the initial mesh and the adaptively refined meshes for $k = 2$ after 10 refinement steps for the classical and the PU localization. A zoom-in highlighting the resulting shapes of adaptively refined elements is provided in Fig. 5.10. The dual problem is treated by a globally higher order discretization, i.e. $z_h^* = z_h^{(k+1)}$. This experiment has been carried out on sequences of meshes, which do not satisfy the condition on the node count. The elements in the initial mesh are triangles. The adaptive process, however, produces naturally polygonal elements during the local refinements. These refinements are located in the expected regions.

The resulting meshes for the experiments with local post-processing for the dual solution, i.e. $z_h^* = \mathfrak{P}_{2h}^{k+1} z_h^{(k)}$, are visualized in Fig. 5.11. As before, a zoom-in highlighting the resulting shapes of adaptively refined elements is provided

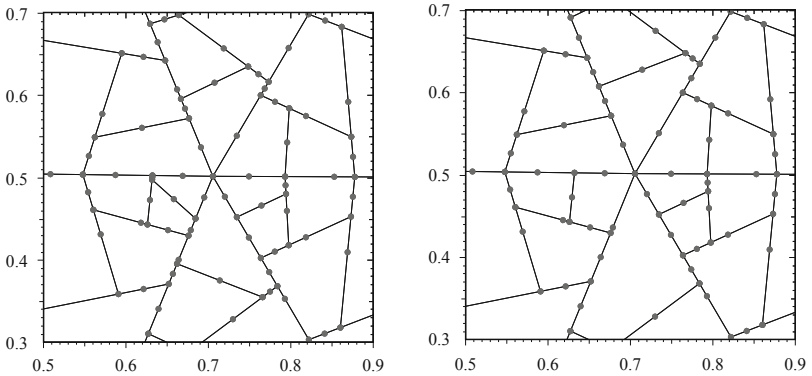

Fig. 5.12 Zoom into L-shaped domain in Problem 3 with adaptive meshes for $k = 2$ after 10 refinements for classical (left) and PU (right) localization, where the dual problem is treated by local post-processing, i.e. $z_h^* = \mathfrak{P}_{2h}^{k+1} z_h^{(k)}$

in Fig. 5.12. This strategy is carried out on a sequence of meshes satisfying the condition on the node count, and thus, the triangular elements in the initial mesh are actually degenerated hexagons. The refinement pattern is similar to the one in Fig. 5.9. But we observe that there are less refinements far from the singularity and the point $\mathbf{x}^*$ after 10 steps. Due to the additional nodes on the boundary of the elements, there are more degrees of freedom per element. Consequently, the approximation over the degenerated hexagonal elements (with triangular shape) is more accurate compared to the corresponding triangular elements in Fig. 5.9.

In order to study convergence, we plot the absolute values of the errors and the estimators with respect to the number of degrees of freedom on a logarithmic scale. The abbreviation $e = u - u_h$ is used in the key of the plots. If we run the computations on a sequence of uniform refined meshes, the convergence slows down due to the singularity located at the reentrant corner. The tests are performed on a uniform sequence $\mathscr{K}_{2h}$, which does not satisfy the condition on the node count, and on a uniform sequence $\mathscr{K}_h$, which satisfies this condition. The initial meshes are visualized in Figs. 5.9 and 5.11, respectively. The corresponding convergence graphs are given in Fig. 5.13 for $k = 1, 2$. In these graphs, the error estimator η^{PU} is given additionally, which clearly reflects the behaviour of the true error $J(e)$.

Next, we apply the adaptive refinement strategy. The following computations are run on meshes satisfying the condition on the node count only. We have performed 25 adaptive refinement steps for the different localization techniques and the two choices of z_h^*. Since $f = 0$ in this test, we directly obtain from (5.12) that $u_{h,B} = 0$ and thus $u_h = u_{h,H} \in V_{h,H}^k$. Consequently, we can reduce the

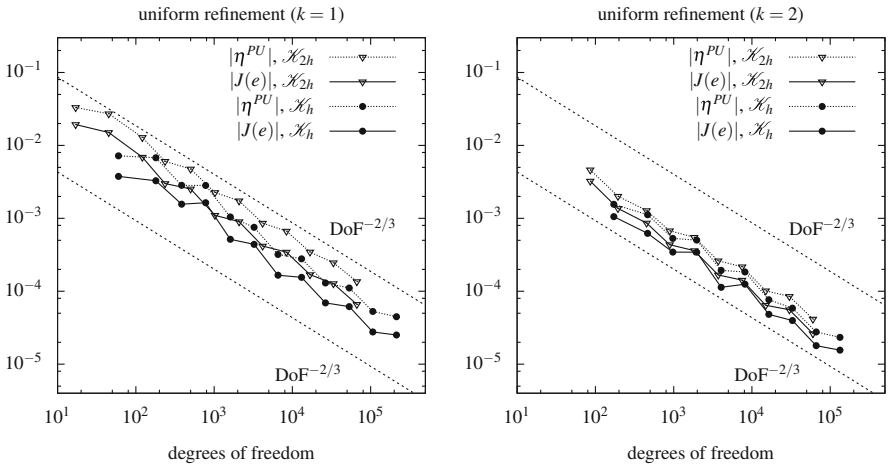

Fig. 5.13 Convergence of uniform refinement strategy with respect to the number of degrees of freedom for Problem 3 with PU localization and $z_h^* = z_h^{(k+1)}$

volume integral in η^{PU} to the boundaries of the elements. Let $K' \in \mathscr{K}_h$ with $K' \subset \omega_K = \text{supp } \chi_K$, it is

$$\left(\nabla u_h, \nabla((z - i_h z)\chi_K)\right)_{L_2(K')} = \left(\gamma_1^{K'} u_h, \gamma_0^{K'}((z - i_h z)\chi_K)\right)_{L_2(\partial K')}$$

according to Green's first identity. This reformulation improved the accuracy of the numerical results. The convergence graphs are given in Fig. 5.14 for the PU localization and in Fig. 5.15 for the classical localization stated in Prop. 5.8. In contrast to the uniform refinement strategy, we recover higher convergence rates, which are not limited by the regularity of the primal solution. Both localization techniques show comparable performance in Figs. 5.14 and 5.15, respectively. The PU localization, however, has a better effectivity while less computational effort is spent for the dual problem. Furthermore, we point out that the convergence is actually faster than expected. Indeed for finite elements, L_∞ regularity results for irregular meshes have been established in [153] and further references to regular meshes are cited therein. In particular, assuming enough regularity, we would expect for $k = 2$ a behaviour like $\mathscr{O}(\mathrm{DoF}^{-3/2})$. For $k = 1$ we would expect $\mathscr{O}(\mathrm{DoF}^{-1})$ including a logarithm term [153]. However in our computations, we observe for $k = 2$ a behaviour like $\mathscr{O}(\mathrm{DoF}^{-3})$. For $k = 1$ the error $J(e)$ seems to converge with $\mathscr{O}(\mathrm{DoF}^{-2})$ rather than with $\mathscr{O}(\mathrm{DoF}^{-1})$ indicated by the estimators η^{PU} and η^{CL}. These effects might be caused by the special meshes, which include additional

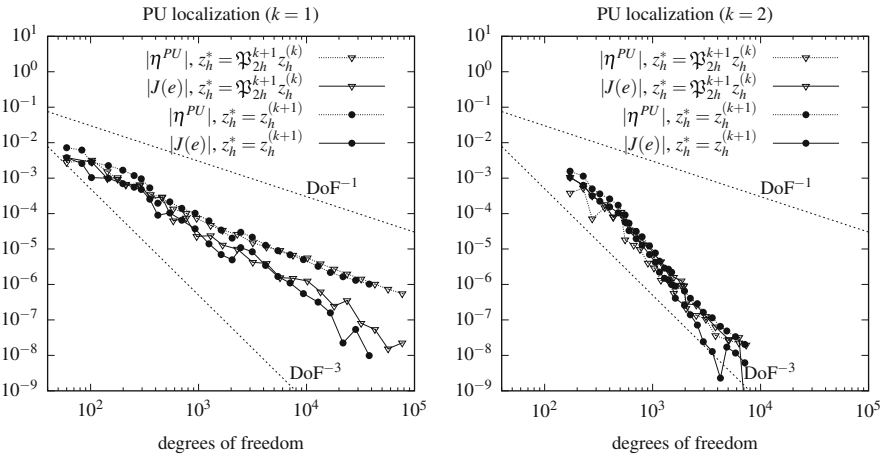

Fig. 5.14 Convergence of adaptive refinement strategy with respect to the number of degrees of freedom for Problem 3 with PU localization

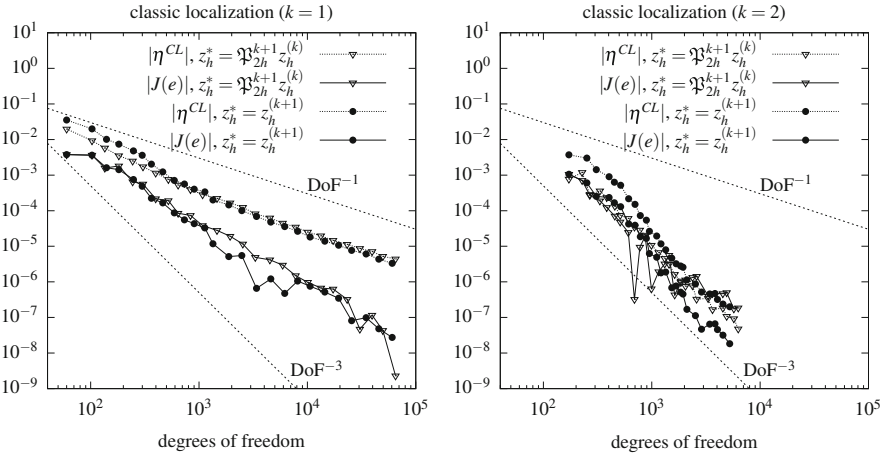

Fig. 5.15 Convergence of adaptive refinement strategy with respect to the number of degrees of freedom for Problem 3 with classic localization

nodes in order to satisfy the condition on the node count during the refinement. Furthermore, the implementation allows edge degeneration, that is excluded in the current theory of most polygonal discretization techniques, but which might be beneficial. These observations rise open questions for future research.